Article

Continuous symmetry breaking in a two-dimensional Rydberg array

https://doi.org/10.1038/s41586-023-05859-2

Received: 21 July 2022

Accepted: 16 February 2023

Published online: 27 February 2023

Check for updates

Cheng Chen[1,13], Guillaume Bornet[1,13], Marcus Bintz[2,13], Gabriel Emperauger[1,13], Lucas Leclerc[1,3], Vincent S. Liu[2], Pascal Scholl[1,4], Daniel Barredo[1,5], Johannes Hauschild[2,6,7], Shubhayu Chatterjee[2], Michael Schuler[8], Andreas M. Läuchli[8,9,10], Michael P. Zaletel[2,11], Thierry Lahaye[1], Norman Y. Yao[2,11,12] & Antoine Browaeys[1]✉

Spontaneous symmetry breaking underlies much of our classification of phases of matter and their associated transitions[1–3]. The nature of the underlying symmetry being broken determines many of the qualitative properties of the phase; this is illustrated by the case of discrete versus continuous symmetry breaking. Indeed, in contrast to the discrete case, the breaking of a continuous symmetry leads to the emergence of gapless Goldstone modes controlling, for instance, the thermodynamic stability of the ordered phase[4,5]. Here, we realize a two-dimensional dipolar XY model that shows a continuous spin-rotational symmetry using a programmable Rydberg quantum simulator. We demonstrate the adiabatic preparation of correlated low-temperature states of both the XY ferromagnet and the XY antiferromagnet. In the ferromagnetic case, we characterize the presence of a long-range XY order, a feature prohibited in the absence of long-range dipolar interaction. Our exploration of the many-body physics of XY interactions complements recent works using the Rydberg-blockade mechanism to realize Ising-type interactions showing discrete spin rotation symmetry[6–9].

Constraints on when and how symmetries can be broken in many-particle systems abound. For example, long-wavelength fluctuations preclude the breaking of continuous symmetries in low-dimensional systems with short-range interactions[10–14]. The presence of long-range interactions qualitatively alters this picture[15]. On the one hand, they can stabilize certain forms of finite-temperature order, which would otherwise be forbidden[16–19]. On the other hand, they can also lead to frustration in which interactions compete with one another, preventing the formation of order[20–24]. Even when order persists in both the short- and long-range cases, the nature of this order, including the dispersion of excitations or the decay of correlation functions, can be fundamentally distinct[18,25–27].

Synthetic quantum systems are ideally suited to study these features. Whereas ultra-cold atoms in optical lattices have investigated continuous symmetry breaking with contact interaction[28], dipolar molecules in lattices[29–32] or trapped ions[33–36] are promising platforms to realize the long-range case. Here, we use a Rydberg quantum simulator to realize a long-range interacting, two-dimensional XY spin system with either ferromagnetic (FM) or antiferromagnetic (AFM) couplings. We arrange up to $N = 100$ dipolar interacting Rydberg atoms into a defect-free square lattice, so that the many-body ground state in either the FM or AFM case is in a continuous symmetry-breaking phase characterized by off-diagonal long-range order (LRO)[37]. For the dipolar XY FM, theory predicts that this continuous symmetry-breaking order persists in the presence of thermal fluctuations[17,18,27]. On the contrary, dipolar interactions are insufficient to stabilize finite temperature LRO in the antiferromagnet[14]. Rather, one expects power-law decaying, algebraic LRO due to Berezinskii–Kosterlitz–Thouless (BKT) physics[38–42].

Our main results are threefold. First, leveraging single-site addressing, we adiabatically prepare correlated low-temperature states of both the XY FM and the XY AFM starting from a classical staggered spin configuration. Second, we characterize the prepared states by measuring the full spatial profile of correlation functions. In the ferromagnet, the system shows correlations consistent with the presence of true LRO: a feature prohibited in conventional short-range-interacting, two-dimensional magnets[12,13]. Meanwhile, in the antiferromagnet, correlations vanish at long distances, consistent with the decay expected from algebraic LRO. We also show that the states produced are not classical FM or AFM. Third, by introducing a partial quench into the adiabatic ramp, we study the robustness of the magnetic order with respect to an excess energy akin to an effective temperature. This allows us to probe the phase diagram of the dipolar XY model (Fig. 1).

The experimental setup (Fig. 1a) consists of a two-dimensional square lattice of ^{87}Rb atoms trapped in an optical tweezer array[8]. We encode an effective spin-1/2 in a pair of opposite-parity Rydberg states, $|\uparrow\rangle = |60S_{1/2}\rangle$ and $|\downarrow\rangle = |60P_{1/2}\rangle$. Resonant dipole–dipole interactions between the spins naturally realize the dipolar XY model[43],

[1]Institute of Optics Graduate School, CNRS, Charles Fabry Laboratory, University of Paris-Saclay, Palaiseau Cedex, France. [2]Department of Physics, University of California, Berkeley, CA, USA. [3]PASQAL SAS, Massy, France. [4]California Institute of Technology, Pasadena, CA, USA. [5]Nanomaterials and Nanotechnology Research Center (CINN-CSIC), University of Oviedo (UO), El Entrego, Spain. [6]Department of Physics, Technical University of Munich, Garching, Germany. [7]Munich Center for Quantum Science and Technology (MCQST), München, Germany. [8]Institute for Theoretical Physics, University of Innsbruck, Innsbruck, Austria. [9]Laboratory for Theoretical and Computational Physics, Paul Scherrer Institute, Villigen, Switzerland. [10]Institute of Physics, Swiss Federal Institute of Technology (EPFL), Lausanne, Switzerland. [11]Materials Sciences Division, Lawrence Berkeley National Laboratory, Berkeley, CA, USA. [12]Department of Physics, Harvard University, Cambridge, MA, USA. [13]These authors contributed equally: Cheng Chen, Guillaume Bornet, Marcus Bintz, Gabriel Emperauger. ✉e-mail: antoine.browaeys@institutoptique.fr

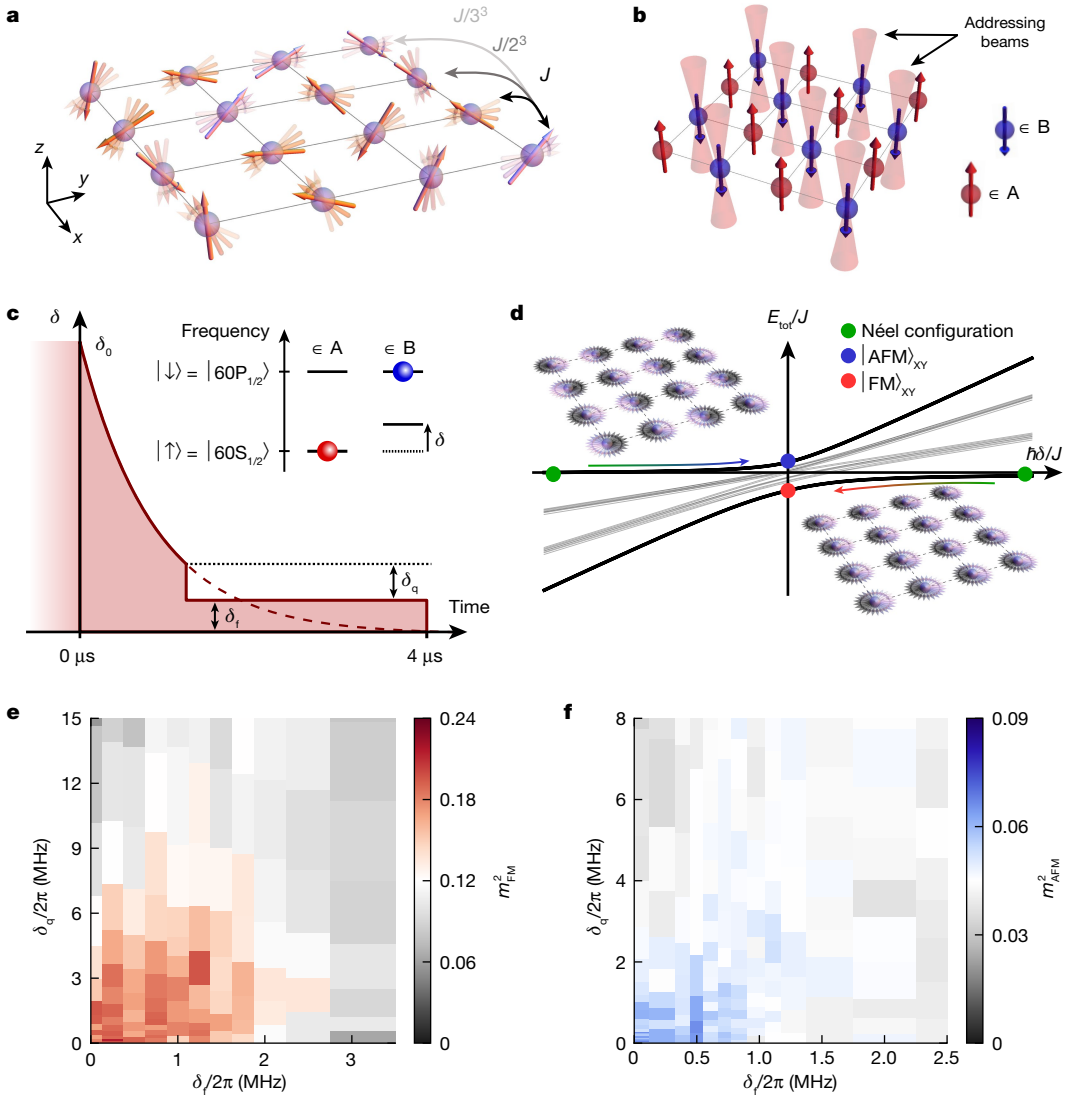

Fig. 1 | Dipolar XY model in a Rydberg quantum simulator and experimental phase diagram. a, Schematic depicting the long-range dipolar XY model. An effective spin is encoded in a pair of Rydberg states that exhibit dipolar flip-flop interactions. **b**, A spatially dependent light shift is used to prepare the system in a Néel spin configuration. **c**, The amplitude δ of the light shift is decreased as a function of time to a final value, δ_f. To study the robustness of the magnetic order with respect to an excess energy, we introduce a diabatic quench of magnitude δ_q. **d**, Energy spectrum of H_{tot} as a function of δ, for $N = 2 \times 3$. When starting in the ground state for $\hbar\delta/J \gg 1$, the system is adiabatically ramped to the FM XY state, pictured by the coloured fluctuating arrows correlated in directions. When starting in the highest excited state for $\hbar\delta/J \ll -1$, the system is adiabatically ramped to the AFM XY state, portrayed by the anticorrelated fluctuating arrows. **e**, FM phase diagram depicting the magnetization squared as a function of the final staggered field strength, δ_f and the diabatic quench magnitude, δ_q. Symmetry breaking is expected in a lobe about ($\delta_f = 0$, $\delta_q = 0$) and is destroyed by either quantum (δ_f) or thermal (δ_q) fluctuations. On a 6×7 system, a crossover between ordered and disordered behaviour is observed. **f**, Analogous phase diagram for the antiferromagnet. Note that at finite temperature, only algebraic LRO is expected.

$$H_{XY} = -\frac{J}{2}\sum_{i<j}\frac{a^3}{r_{ij}^3}(\sigma_i^x\sigma_j^x + \sigma_i^y\sigma_j^y), \quad (1)$$

where σ_i^α are Pauli matrices, r_{ij} is the distance between spins i and j, $J/h = 0.77$ MHz is the dipolar interaction strength and $a = 12.5$ μm is the lattice spacing; here, the quantization axis is defined by an external magnetic field perpendicular to the lattice plane, which ensures that the dipolar interactions are isotropic. The Hamiltonian shows a continuous $U(1)$ symmetry corresponding to the conservation of total z magnetization, $M^z = \sum_i \sigma_i^z$ (Methods and Extended Data Fig. 1).

The starting point of our experiments is a classical Néel spin configuration, that is, a staggered arrangement of spins $|\downarrow\rangle$ and $|\uparrow\rangle$ with $M^z = 0$, prepared in the following way (Methods): after initializing all the atoms in $|\uparrow\rangle$, we apply focused laser beams to produce spatially dependent light shifts, implementing the Hamiltonian $H_Z = \hbar\delta\sum_i n_i$. The n_i form a staggered pattern with $n_i = 0$ on the A sublattice and $n_i = (1 + \sigma_i^z)/2$ on the B sublattice (Fig. 1b). We then sweep a global microwave pulse across the resonance of the atoms in the A sublattice that flips their spin to $|\downarrow\rangle$. This leads to the Néel configuration, which is a good approximation of the ground state (for $\delta > 0$) or highest excited state (for $\delta < 0$) of the total Hamiltonian $H_{tot} = H_{XY} + H_Z$ for $\hbar|\delta| \gg J$.

Starting from this configuration, we dynamically prepare highly correlated, quantum many-body states by ramping down as a function of time the laser field producing the staggered light shifts, either abruptly or adiabatically (Fig. 1c) (for a discussion of an alternative preparation approach, see Methods and Extended Data Fig. 5). In the adiabatic case, for $\delta(t) > 0$, the ramp connects the Néel configuration

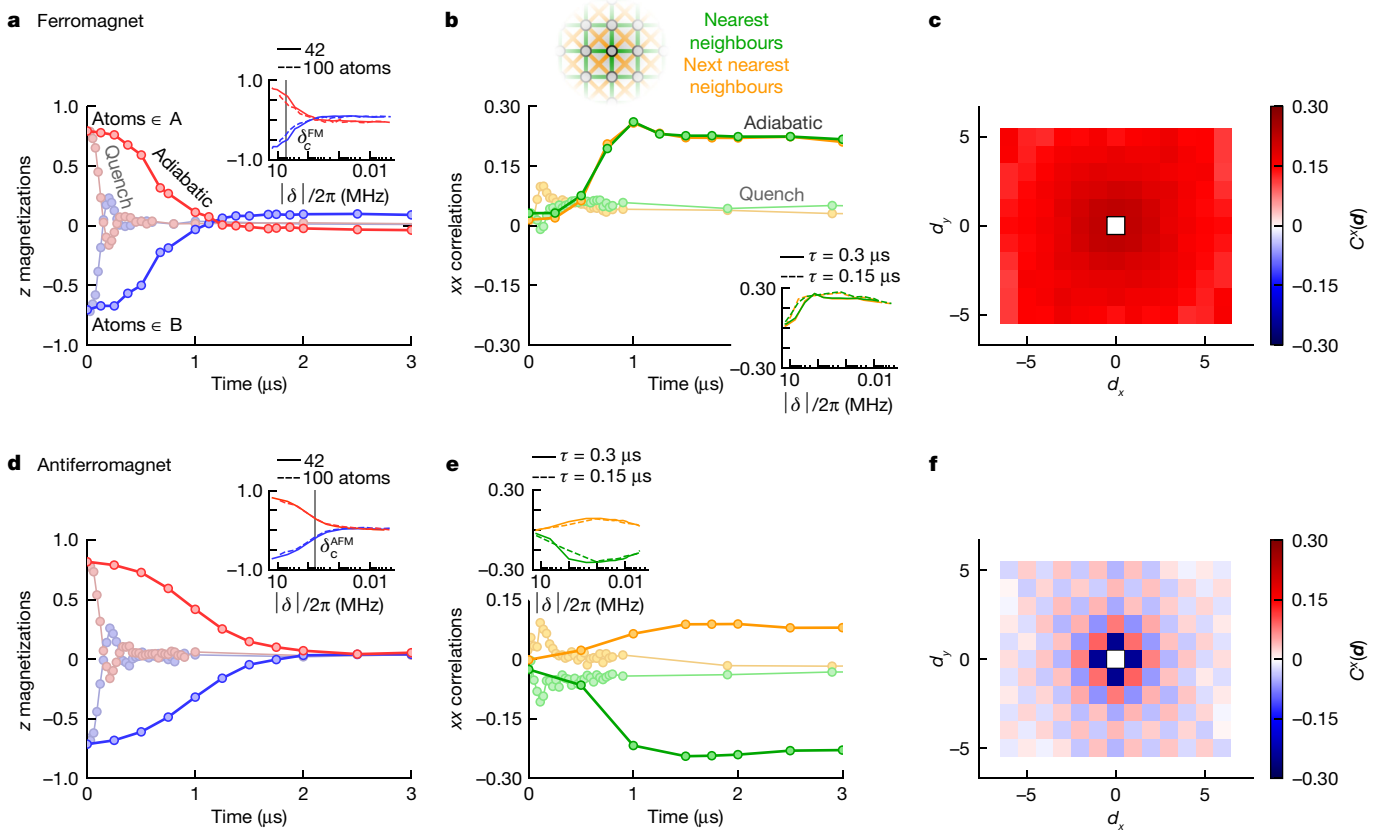

Fig. 2 | Adiabatic preparation of dipolar XY ferro- and antiferromagnets. **a**, Sublattice-resolved magnetization $\langle\sigma_i^z\rangle$ as the staggered field $\delta(t)$ is reduced. At $t = 0$, the state is prepared in a classical Néel state along the z axis, as indicated by the opposing magnetization of atoms in the A (red) and B (blue) sublattices. As the staggered field $\delta(t)$ is turned off, either adiabatically or by means of a sudden quench, the Néel magnetization decays towards zero. Inset: comparison of the z magnetizations decay as a function of δ for a 6×7 versus a 10×10 lattice. The grey vertical line indicates the value δ_c^{FM} in which the phase transition occurs, inferred from the theory (Methods). **b**, The formation of a low-energy XY ferromagnet is detected by the in-plane two-point correlation function, $C_{i,j}^x$. Data are shown for i,j averaged over either nearest or next-nearest pairs. The sudden quench produces more energy that destroys the XY order and leads to correlations near zero. Inset: nearest and next-nearest correlations for two different adiabatic ramp rates. **c**, The xx correlations as a function of displacement, $C^x(\mathbf{d}) \equiv \langle C_{\mathbf{r},\mathbf{r}+\mathbf{d}}^x\rangle_{\mathbf{r}}$, measured at time, $t = 2$ μs (with d_x and d_y in units of lattice spacing a). **d**–**f**, Analogous results to **a**–**c**, respectively, for the AFM case. Crucially (**e**,**f**), we observe staggered correlations.

to the low-temperature FM states of H_{XY}, as shown in Fig. 1d. Meanwhile, for $\delta(t) < 0$, the adiabatic ramp prepares negative-temperature states of H_{XY} or equivalently, low-temperature AFM states of $-H_{XY}$ (Fig. 1d)[44]. In the thermodynamic limit of both cases, a quantum phase transition (QPT) is expected to occur at some critical $\delta_c^{FM/AFM}$, between the Néel configuration and the XY order (Methods and Extended Data Fig. 4).

To investigate the XY ferromagnet, we begin with a 6×7 lattice and use an exponential ramp profile, $\delta(t) \approx \delta_0 e^{-t/\tau}$, with $\delta_0 = 2\pi \times 15$ MHz and $\tau = 0.3$ μs. As depicted in Fig. 2a, for both sublattices, the on-site z magnetization, $2\sum_{i\in A/B}\langle\sigma_i^z\rangle/N$, obtained by averaging over many realizations of the experiment, decreases towards zero, with a residual late-time offset arising from experimental imperfections (Methods). This is consistent with the XY ferromagnet, which orders in the equatorial plane, but by itself, is insufficient to diagnose the phase. Indeed, quenching the staggered light shifts (in less than 100 ns) leads to a near infinite temperature state, which also shows a magnetization that rapidly relaxes to zero (lighter curves, Fig. 2a).

The key characteristic of the XY ferromagnet is only revealed upon measuring the correlation function, $C_{i,j}^x = \langle\sigma_i^x\sigma_j^x\rangle - \langle\sigma_i^x\rangle\langle\sigma_j^x\rangle$ (Methods). For the quenched state, the correlation functions remain near zero for all times, consistent with high-temperature behaviour (lighter curves, Fig. 2b). The dynamics of the adiabatic protocol are markedly distinct: both nearest-neighbour and next-nearest-neighbour correlations grow to a stable non-zero value at late times, indicative of order[37].

By switching the sign of δ_0, we also investigate the XY antiferromagnet. Both the z magnetization (Fig. 2d) and the correlation functions (Fig. 2e) show qualitatively similar dynamics to the FM case. One notable difference is that $C^x < 0$ for nearest-neighbour correlations, indicating that neighbouring spins have anti-aligned.

A few remarks are in order. First, to explore the adiabaticity of our protocol, we vary the time-constant of the exponential ramp. As shown in the insets of Fig. 2b,e, the dynamics of the correlation function agree between $\tau = 0.15$ and $\tau = 0.3$ μs, indicating that diabatic errors are not a limiting factor. We confirm this by numerical simulation of the many-body dynamics (Methods and Extended Data Fig. 7). Second, whereas the long-range tail of the dipolar interaction reinforces the XY FM order, it is weakly frustrating for the AFM[15]. As a consequence, the phase transition between the Néel configuration and the XY AFM is expected to occur at a smaller value of the staggered light shift as compared to the XY FM, that is, $|\delta_c^{AFM}| < |\delta_c^{FM}|$ (Methods). This is indeed borne out by the data in which we observe that the magnetization decays to zero faster as a function of δ for the FM case than for the AFM. Third, we increase the system size to a 10×10 lattice and perform the analogous adiabatic preparation protocols. We find the same behaviour for all observables (insets, Fig. 2a,d), indicating that our results are robust to finite-size effects[45]. Finally, we observe that at the latest times, the correlations in both the FM and AFM cases show a slow decay; we conjecture that this decay arises from a combination of residual atomic

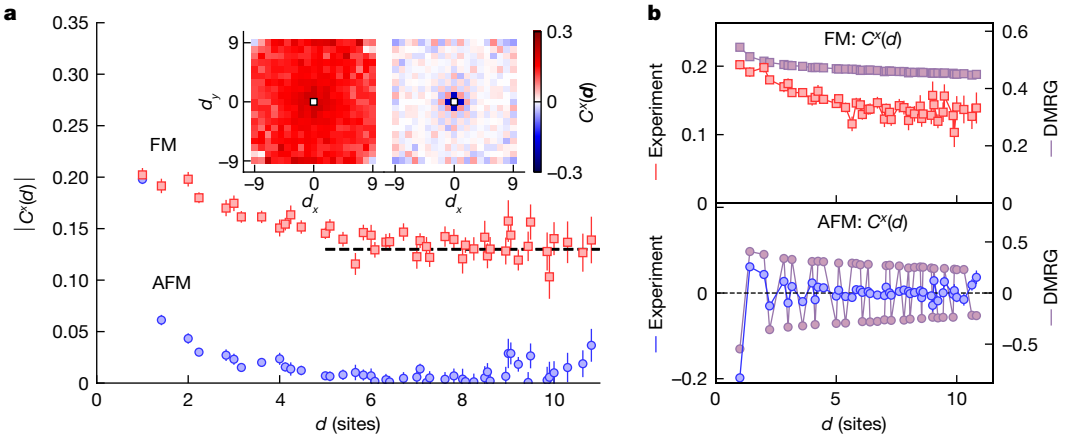

Fig. 3 | Observing long-range XY order in a 10 × 10 lattice. a, The xx correlations averaging over displacements of the same distance, $C^x(d)$. The XY ferromagnet shows a plateau consistent with LRO, whereas the XY antiferromagnet shows a decay to zero. Inset: spatial correlations as a function of displacement, measured at time $t = 1$ µs. **b**, Comparison of the experimental data shown in **a** with the ground-state results obtained from DMRG.

motion and the finite lifetime of the Rydberg states (more details are in Methods).

Our measurements of the local correlations suggest we have dynamically prepared low-temperature states of the XY FM and AFM, but are these states truly long-range ordered? To investigate this, we measure the long-distance spin-spin correlations of the system after adiabatic preparation. In Fig. 2c,f (6 × 7) and Fig. 3a (10 × 10) we show the correlations as a function of the displacement $\mathbf{d}$, averaging over initial positions: $C^x(\mathbf{d}) \equiv \langle C^x_{\mathbf{r},\mathbf{r}+\mathbf{d}} \rangle_{\mathbf{r}}$. The FM correlations are of constant sign and seem to plateau at long distances, indicative of LRO, whereas the AFM correlations are staggered and show a decay. For a more quantitative assessment, we focus on the 10 × 10 array and plot $C^x(d)$, averaging over displacements of the same distance $d = |\mathbf{d}|$. In the XY AFM, correlations decay to zero at large distances, indicating the absence of LRO. By contrast, the XY FM indeed shows a plateau, $C^x_\infty \approx 0.13$, which establishes it as a magnetically ordered state with an effective magnetization density $m_{\mathrm{eff}} \equiv \sqrt{2C^x_\infty} = 0.51$ (Methods).

For further insight, in Fig. 3b we compare the measured $C^x(d)$ against the exact ground-state prediction obtained from density matrix renormalization group (DMRG) calculations (Methods)[46,47]. In the DMRG ground state, $C^x(d)$ does plateau in the FM, but slowly decays in the AFM due to finite-size effects; in the thermodynamic limit, both the FM and AFM ground states are expected to be long-range ordered at zero temperature. The qualitative structure of the measured $C^x(d)$ (for example, sign structure in the AFM case) is consistent with theory, but the experimental correlations are weaker. Several effects could contribute to this. For example, the finite fidelity of the initial Néel state introduces an entropy density (that is, an effective finite temperature). This is especially destructive to the AFM, for which finite-temperature LRO is forbidden[14,15], in agreement with our observation. Other experimental imperfections including read-out errors are discussed in the Methods; including these errors in our numerical simulations leads to excellent agreement with the data for the 6 × 7 lattice (Methods and Extended Data Fig. 6). However, we also observe that running the adiabatic preparation protocol to longer timescales leads to extra decoherence that adversely affects the FM magnetization plateau in a non-trivial fashion; in particular, correlations at the largest distances begin to decay before their shorter-distance counterparts (Methods and Extended Data Fig. 3).

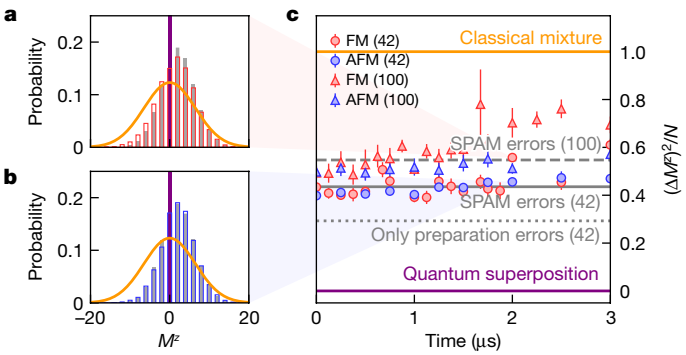

Fig. 4 | Analysis of the z magnetization during the adiabatic ramp. **a**,**b**, Experimental histograms of the z magnetization M^z ($N = 42$) for the FM (**a**) and AFM (**b**) case together with the ideal case (purple), and the expected distribution including SPAM errors (grey bars). The orange line is the binomial distribution corresponding to a classical magnet (text). **c**, Normalized variance $(\Delta M^z)^2/N$ as a function of time during the ramp, for the experiment (circles for $N = 42$, triangles for $N = 100$), the classical magnet (orange line) and a perfect XY-magnet (purple line). The grey continuous and dashed lines show the ideal case including SPAM errors. The dotted line shows the ideal case ($N = 42$) including only state preparation errors.

As a final characterization of the prepared states, we investigate whether each realization of the experiment produces a classical magnet pointing in a random direction θ in the xy plane or a genuinely quantum many-body state (Methods). To do so, we analyse the statistical distribution of M^z, which is conserved during the adiabatic ramp. For a classical FM or AFM, each spin, aligned or anti-aligned along θ, is an equal superposition of $|\uparrow\rangle$ and $|\downarrow\rangle$, so that M^z follows a binomial distribution. By contrast, the ground state of H_{XY} is an eigenstate of M^z, and its variance should be zero. Figure 4a,b shows experimental histograms of the z magnetization at $t = 2$ µs for the FM and AFM. Figure 4c presents the variance for various times t. We find that the states have a variance smaller than that of a binomial distribution, indicating that we do not prepare classical magnets. In fact, the measured non-zero variances can be fully explained by the state preparation and measurement (SPAM) errors applied to the ideal distribution (Methods, Extended Data Fig. 2, and Extended Data Table 1). We have also checked the rotation invariance of the state around z by measuring the magnetization along y and finding the same as along x. Altogether, our measurements suggest a state that is a coherent quantum superposition over a continuous family of classical configurations (Methods). For such a state, the defining signature of continuous symmetry-breaking order is a long-distance plateau in the correlation function $C^x(d)$, as we observed in the XY FM[5].

As mentioned earlier, the LRO observed in the FM case should persist at finite temperature. We therefore investigate the stability of the

prepared magnetic orders as a function of an effective temperature. To do so, we insert a partial quench of amplitude δ_q into the ramp, followed by an equilibration time of at least 1 μs at a final value δ_f of the staggered field (Fig. 1d): the variable quench introduces excess energy into the system, and we observe a relaxation of the magnetization and correlations during the equilibration time. We will use the amplitude of the quench, δ_q, as a proxy for the final effective temperature (Methods and Extended Data Fig. 8). After each $\{\delta_f, \delta_q\}$ ramp, we measure the in-plane magnetization squared, $m^2_{FM/AFM} = \sum_{ij} (\pm 1)^{i+j} C^x_{ij}/N^2$ and construct the phase diagram shown in Fig. 1e,f. Starting with the ferromagnet, for small values of δ_f and δ_q (corresponding to low effective temperatures), the magnetization per site is of $\mathcal{O}(1)$, consistent with the ordered phase (Fig. 1e). As either δ_f or δ_q increases, the magnetization density decreases towards zero indicating melting into a disordered phase. This is consistent with theoretical expectations, where δ_q drives the transition through thermal fluctuations[17], while δ_f tunes across the QPT. We perform the same analysis for the antiferromagnet (Fig. 1f). Compared to the XY ferromagnet, we find that a much smaller region of the $\{\delta_f, \delta_q\}$ phase space shows significant AFM correlations, consistent with the frustration induced by the long-range interactions that destabilizes the phase.

Looking forwards, our work opens the door to several future directions. First, it would be interesting to investigate the nature of the phase transition between the disordered and XY-ordered phases; this will require overcoming several technical challenges including scaling to larger system sizes. Second, the ability to directly prepare low-temperature states in different M^z magnetization sectors suggests the possibility of directly observing the so-called Anderson tower of states, which underlies continuous symmetry breaking in finite quantum systems[48–51]; the structure of these states has led to recent predictions for scalable spin squeezing by quenching in the FM XY phase[52]. Finally, combining optical tweezer geometries that show frustration (such as triangular or kagome lattices) with AFM interactions leads to a rich landscape for exploring frustrated magnetism and spin liquid physics[20,22].

Online content

Any methods, additional references, Nature Portfolio reporting summaries, source data, extended data, supplementary information, acknowledgements, peer review information; details of author contributions and competing interests; and statements of data and code availability are available at https://doi.org/10.1038/s41586-023-05859-2.

1. Landau, L. D. On the theory of phase transitions. I. *Zh. Eksp. Teor. Fiz.* **11**, 19 (1937).
2. Landau, L. D. & Ginzburg, V. L. On the theory of superconductivity. *Zh. Eksp. Teor. Fiz.* **20**, 1064 (1950).
3. Kepler, J. *De Nive Sexangula* (Gottfried Tampach, 1611).
4. Goldstone, J. Field theories with 'Superconductor' solutions. *Il Nuovo Cimento* **19**, 154–164 (1961).
5. Tasaki, H. *Physics and Mathematics of Quantum Many-Body Systems* (Springer International Publishing, 2020).
6. Schauß, P. et al. Crystallization in Ising quantum magnets. *Science* **347**, 1455–1458 (2015).
7. Guardado-Sanchez, E. et al. Probing the quench dynamics of antiferromagnetic correlations in a 2D quantum Ising spin system. *Phys. Rev. X* **8**, 021069 (2018).
8. Scholl, P. et al. Quantum simulation of 2D antiferromagnets with hundreds of Rydberg atoms. *Nature* **595**, 233–238 (2021).
9. Ebadi, S. et al. Quantum phases of matter on a 256-atom programmable quantum simulator. *Nature* **595**, 227–232 (2021).
10. Bloch, F. Zur Theorie des Ferromagnetismus. *Zeitschrift Phys.* **61**, 206–219 (1930).
11. Peierls, R. Quelques propriétés typiques des corps solides. *Annales de l'institut Henri Poincaré* **5**, 177–122 (1935).
12. Mermin, N. D. & Wagner, H. Absence of ferromagnetism or antiferromagnetism in one- or two-dimensional isotropic Heisenberg models. *Phys. Rev. Lett.* **17**, 1133–1136 (1966).
13. Hohenberg, P. C. Existence of long-range order in one and two dimensions. *Phys. Rev.* **158**, 383–386 (1967).
14. Bruno, P. Absence of spontaneous magnetic order at nonzero temperature in one- and two-dimensional Heisenberg and XY systems with long-range interactions. *Phys. Rev. Lett.* **87**, 137203 (2001).
15. Defenu, N. et al. Long-range interacting quantum systems. Preprint at https://arxiv.org/abs/2109.01063 (2021).
16. Dyson, F. J. Existence of a phase-transition in a one-dimensional Ising ferromagnet. *Commun. Math. Phys.* **12**, 91–107 (1969).
17. Kunz, H. & Pfister, C. E. First order phase transition in the plane rotator ferromagnetic model in two dimensions. *Commun. Math. Phys.* **46**, 245–251 (1976).
18. Maleev, S. V. Dipole forces in two-dimensional and layered ferromagnets. *Soviet J. Exp. Theor. Phys.* **43**, 1240 (1976).
19. Fröhlich, J., Israel, R., Lieb, E. H. & Simon, B. Phase transitions and reflection positivity. I. General theory and long range lattice models. *Commun. Math. Phys.* **62**, 1–34 (1978).
20. Diep, H. T. (ed.) *Frustrated Spin Systems* 2nd edn (World Scientific, 2013).
21. Castelnovo, C., Moessner, R. & Sondhi, S. L. Magnetic monopoles in spin ice. *Nature* **451**, 42–45 (2008).
22. Yao, N. Y., Zaletel, M. P., Stamper-Kurn, D. M. & Vishwanath, A. A quantum dipolar spin liquid. *Nat. Phys.* **14**, 405–410 (2018).
23. Keleş, A. & Zhao, E. Absence of long-range order in a triangular spin system with dipolar interactions. *Phys. Rev. Lett.* **120**, 187202 (2018).
24. Keleş, A. & Zhao, E. Renormalization group analysis of dipolar Heisenberg model on square lattice. *Phys. Rev. B* **97**, 245105 (2018).
25. De'Bell, K., MacIsaac, A. B. & Whitehead, J. P. Dipolar effects in magnetic thin films and quasi-two-dimensional systems. *Rev. Mod. Phys.* **72**, 225–257 (2000).
26. Taroni, A., Bramwell, S. T. & Holdsworth, P. C. W. Universal window for two-dimensional critical exponents. *J. Phys. Condens. Matter* **20**, 275233 (2008).
27. Peter, D., Müller, S., Wessel, S. & Büchler, H. P. Anomalous behavior of spin systems with dipolar interactions. *Phys. Rev. Lett.* **109**, 025303 (2012).
28. Mazurenko, A. et al. A cold-atom Fermi-Hubbard antiferromagnet. *Nature* **545**, 462–466 (2017).
29. Yan, B. et al. Observation of dipolar spin-exchange interactions with lattice-confined polar molecules. *Nature* **501**, 521–525 (2013).
30. Christakis, L. et al. Probing site-resolved correlations in a spin system of ultracold molecules. *Nature* **614**, 64–69 (2023).
31. Chomaz, L. et al. Dipolar physics: a review of experiments with magnetic quantum gases. *Rep. Prog. Phys.* **86,** 026401 (2022).
32. Leo, N. et al. Collective magnetism in an artificial 2D XY spin system. *Nat. Commun.* **9**, 2850 (2018).
33. Richerme, P. et al. Non-local propagation of correlations in quantum systems with long-range interactions. *Nature* **511**, 198–201 (2014).
34. Jurcevic, P. et al. Quasiparticle engineering and entanglement propagation in a quantum many-body system. *Nature* **511**, 202–205 (2014).
35. Maghrebi, M. F., Gong, Z.-X. & Gorshkov, A. V. Continuous symmetry breaking in 1D long-range interacting quantum systems. *Phys. Rev. Lett.* **119**, 023001 (2017).
36. Feng, L. et al. Continuous symmetry breaking in a trapped-ion spin chain. Preprint at https://arxiv.org/abs/2211.01275 (2022).
37. Yang, C. N. Concept of off-diagonal long-range order and the quantum phases of liquid He and of superconductors. *Rev. Mod. Phys.* **34**, 694–704 (1962).
38. Berezinskiĭ, V. L. Destruction of long-range order in one-dimensional and two-dimensional systems having a continuous symmetry group I. Classical systems. *Soviet J. Exp. Theor. Phys.* **32**, 493 (1971).
39. Berezinskiĭ, V. L. Destruction of long-range order in one-dimensional and two-dimensional systems possessing a continuous symmetry group. II. Quantum systems. *Soviet J. Exp. Theor. Phys.* **34**, 610 (1972).
40. Kosterlitz, J. M. & Thouless, D. J. Ordering, metastability and phase transitions in two-dimensional systems. *J. Phys. C. Solid State Phys.* **6**, 1181–1203 (1973).
41. Kosterlitz, J. M. The critical properties of the two-dimensional XY model. *J. Phys. C Solid State Phys.* **7**, 1046–1060 (1974).
42. Giachetti, G., Defenu, N., Ruffo, S. & Trombettoni, A. Berezinskii-Kosterlitz-Thouless phase transitions with long-range couplings. *Phys. Rev. Lett.* **127**, 156801 (2021).
43. Browaeys, A. & Lahaye, T. Many-body physics with individually controlled Rydberg atoms. *Nat. Phys.* **16**, 132 (2020).
44. Sørensen, A. S. et al. Adiabatic preparation of many-body states in optical lattices. *Phys. Rev. A.* **81**, 061603 (2010).
45. Sandvik, A. W. & Hamer, C. J. Ground-state parameters, finite-size scaling, and low-temperature properties of the two-dimensional S = 1/2 XY model. *Phys. Rev. B* **60**, 6588–6593 (1999).
46. White, S. R. Density matrix formulation for quantum renormalization groups. *Phys. Rev. Lett.* **69**, 2863–2866 (1992).
47. Hauschild, J. & Pollmann, F. Efficient numerical simulations with tensor networks: Tensor Network Python (TeNPy). *SciPost Physics Lecture Notes* 5 (2018).
48. Anderson, P. W. An approximate quantum theory of the antiferromagnetic ground state. *Phys. Rev.* **86**, 694–701 (1952).
49. Anderson, P. W. *Basic Notions of Condensed Matter Physics* (Perseus Publishing, 2010).
50. Tasaki, H. Long-range order, 'tower' of states, and symmetry breaking in lattice quantum systems. *J. Stat. Phys.* **174**, 735–761 (2019).
51. Beekman, A., Rademaker, L. & van Wezel, J. An introduction to spontaneous symmetry breaking. *SciPost Physics Lecture Notes* 11 (2019).
52. Comparin, T., Mezzacapo, F. & Roscilde, T. Robust spin squeezing from the tower of states of U(1)-symmetric spin Hamiltonians. *Phys. Rev. A* **105**, 022625 (2022).

Methods

Experimental methods

The realization of the dipolar XY model relies on our ^{87}Rb Rydberg-atom tweezer array setup, described in previous works[8,53,54]. The pseudo-spin states are $|\uparrow\rangle = |60S_{1/2}, m_j = 1/2\rangle$ and $|\downarrow\rangle = |60P_{1/2}, m_j = -1/2\rangle$. We manipulate them using resonant microwaves at 16.7 GHz. A $\cong$ 50 Gauss magnetic field, perpendicular to the array, defines the quantization axis (Extended Data Fig. 1a) and shifts away the irrelevant Zeeman states of the $60S_{1/2}$ and $60P_{1/2}$ manifolds.

Addressability in the tweezer array. The addressing laser pattern used to prepare the initial classical Néel configuration is generated by a 1,013 nm laser beam detuned from the transition between the intermediate state $6P_{3/2}$ and $|\uparrow\rangle$ (Extended Data Fig. 1b). The sign of the detuning sets the one of the light shift: in the FM (respectively AFM) case, the frequency of the addressing laser is tuned below (resp. above) the resonance by roughly 250 MHz.

We use a dedicated spatial light modulator to produce the pattern of addressing beams. Each beam is focused on a $1/e^2$ radius of about 1.5 μm, for a typical power of 60 mW. We measure the light shift for each addressed atom by microwave spectroscopy on the $|\uparrow\rangle - |\downarrow\rangle$ transition. The average light shift is $|\delta_0| = 2\pi \times 15$ MHz over the 42-atom array (21 addressed atoms), and $|\delta_0| = 2\pi \times 9$ MHz over the 100-atom array (50 addressed atoms). These values are dictated by available laser power. For both arrays, the rms dispersion of δ_0 across the addressing beams is 2.4%.

Experimental sequence. The experimental sequence is shown in Extended Data Fig. 1. After assembling the array[53] we use Raman sideband cooling along the radial directions of the tweezers, and reach a temperature of 10 μK. We then optically pump the atoms in $|g\rangle = |5S_{1/2}, F = 2, m_F = 2\rangle$ before adiabatically ramping down the tweezer depth by a factor of roughly 40. Following this, we switch off the tweezers, and excite the atoms to $|\uparrow\rangle$ using a two-photon stimulated Raman adiabatic passage (STIRAP) with 421 and 1,013 nm lasers (roughly 2 μs duration).

To generate the classical Néel configuration along z, we first transfer all the atoms from $|\uparrow\rangle$ to $|\downarrow\rangle$ using a 54 ns microwave π pulse. Subsequently, the addressing beams are applied to the atoms in sublattice B. We then transfer the atoms A from $|\downarrow\rangle$ back to $|\uparrow\rangle$ by an adiabatic microwave sweep while the atoms B remain in $|\downarrow\rangle$, as illustrated in Extended Data Fig. 1b. In this procedure, exciting first the atoms in $|\downarrow\rangle$ has the advantage of minimizing the depumping of the $|\uparrow\rangle$ atoms by the addressing light (Decoherence during the adiabatic ramp). An example of perfect Néel configuration obtained at the end of the preparation is shown in Extended Data Fig. 1c.

The experimental sequence (including the detection part detailed in the next section) is repeated typically over 1,000 defect-free assembled arrays. This allows us to calculate the magnetization and the spin correlations by averaging over these realizations.

State detection procedure. At the end of the sequence, we read out the state of each atom in the natural z basis. To do so, we de-excite the atoms from $|\uparrow\rangle$ to the $5S_{1/2}$ manifold where they are recaptured in the tweezers and imaged. Thus, the $|\uparrow\rangle$ (resp. $|\downarrow\rangle$) state is mapped to the presence (resp. absence) of the corresponding atom. To avoid the detrimental effects of the $|\uparrow\rangle - |\downarrow\rangle$ interaction-induced dynamics during the deexcitation, we freeze out the system by shelving the $|\downarrow\rangle$ atoms to $|D\rangle = |59D_{3/2}, m_j = -1/2\rangle$ where they hardly interact with the ones in $|\uparrow\rangle$. This is achieved by using a 48 ns microwave π pulse at 10.6 GHz. The subsequent deexcitation is performed by applying a 2.5 μs light pulse resonant with the transition between $|\uparrow\rangle$ and the short-lived intermediate state $6P_{3/2}$ from which the atoms decay back to $5S_{1/2}$. Furthermore, when we want to measure the spins along x we rotate them by applying a 27 ns microwave $\pi/2$-pulse on the $|\uparrow\rangle - |\downarrow\rangle$ transition before the detection. However, this procedure is efficient only for light shifts $|\delta(t)|$ much smaller than the microwave Rabi frequency, that is, for times larger than roughly 0.5 μs during an adiabatic preparation.

Experimental imperfections

The sequences described above are affected by experimental imperfections. As taking all of them into account is intractable, we estimate here the effect of the main imperfections on the quantities we measure. We first analyse the SPAM errors and then discuss decoherence in the system.

SPAM errors. To estimate the SPAM errors, we break down the sequence into a series of steps i, each having a small but finite failure probability η_i. In the following, we keep only the contributions of imperfections to first order in the η_is.

As an example, we show in Extended Data Fig. 2 the discretized sequence corresponding to the preparation and measurement of the classical Néel configuration (corresponding to the time $t = 0$ in Fig. 2a). Extended Data Table 1 gives the corresponding values of the probabilities η_i for 42 atoms, that are either inferred from a series of dedicated experiments or estimated from numerical simulations. The table also mentions the physical origin of these imperfections.

For atoms in sublattice A (non-addressed), the error tree leads to the probability to recapture the atoms at the end of the sequence, which reads (to first order):

$$P_z^{\mathrm{A}} \approx 1 - \eta_{\mathrm{MW}} - \eta_{\mathrm{A}} - \eta_{\mathrm{dx}} - \epsilon. \tag{2}$$

Similarly, the calculation for sublattice B (addressed atoms) yields:

$$P_z^{\mathrm{B}} \approx \eta_{\mathrm{STIRAP}} + \eta_{\mathrm{B}} + \epsilon'. \tag{3}$$

Using the values reported in Extended Data Table 1, we obtain $P_z^{\mathrm{A}} = 0.90$, $P_z^{\mathrm{B}} = 0.15$. From these probabilities, we compute an initial magnetization along z, $\sigma_z^{\mathrm{A}} = 2P_z^{\mathrm{A}} - 1 = 0.8$ and $\sigma_z^{\mathrm{B}} = 2P_z^{\mathrm{B}} - 1 = -0.70$. We checked that these values agree with measured magnetizations at $t = 0$, which are used as a calibration of the errors, for both the FM and the AFM (Fig. 2a,d). Finally, the error tree allows us to infer the probability of successful initial preparation per spin. We find 0.87 for the atoms in sublattice A and 0.92 for the ones in B. Using the preparation part of the error tree (Extended Data Fig. 2), we find $1 - \eta_{\mathrm{STIRAP}} - \eta_{\mathrm{MW}} - \eta_{\mathrm{A}} = 0.89$ for the atoms in sublattice A and $1 - \eta_{\mathrm{STIRAP}} - \eta_{\mathrm{MW}} - \eta_{\mathrm{B}} = 0.88$ for the ones in B. These values are very similar to the ones including detection errors, indicating that this experiment is dominated by preparation errors.

Decoherence during the adiabatic ramp. Besides the SPAM errors described previously, further imperfections lead to decoherence.

First, we focus on the long-time behaviour of the magnetizations for the 10 × 10 arrays. In Fig. 2a, one observes that, in the FM case, the z magnetizations of sublattices A and B do not vanish at late times, but reach a constant finite value of a few percent. By contrast, this does not occur in the AFM case (Fig. 2d). We qualitatively explain this effect by the following observations. First, because of off-resonant scattering by the addressing beam, atoms in $|\uparrow\rangle$ are slowly depumped to the ground state $|g\rangle$; we have measured the effective lifetime of an addressed $|\uparrow\rangle$ atom to be around 4 μs, whether the light shift is $2\pi \times 15$ or $-2\pi \times 15$ MHz (so that this alone, cannot explain the difference between the FM and AFM cases). However, during our adiabatic ramp down of light-shift $\delta(t)$, the addressed atoms are initially in $|\downarrow\rangle$ (and thus cannot be depumped). Depumping sets in only when the system enters the ordered phase, where an addressed atom has a significant probability of being in $|\uparrow\rangle$. As $\delta_{\mathrm{c}}^{\mathrm{AFM}} < \delta_{\mathrm{c}}^{\mathrm{FM}}$, the addressing beam intensity (and thus the depumping rate) is at this stage much smaller for the AFM case than for the FM case, and thus has a negligible effect in the former case.

Second, we investigate the role of decoherence on the appearance of LRO along x in the FM case, for the 10×10 array. Extended Data Fig. 3a shows the time evolution of the nearest-neighbour correlations as we ramp down the light shift, all the way up to 8 μs (in contrast with Fig. 2b of the main text where the evolution is shown only up to 3 μs, and for 42 atoms). Two timescales appear: first, correlations build up until $t \simeq 1$ μs as the FM state is adiabatically prepared and then, they slowly decay and lose 25% of their value in 7 μs. This decay is not expected, because the system should be ideally in steady state once it has reached the FM phase. We conjecture that the experimental system is affected by decoherence arising from a combination of the residual atomic motion and spontaneous emission from the Rydberg states.

To further analyse the evolution of the FM order, we probe the full spatial structure of the correlations at different times. Extended Data Fig. 3b summarizes the results. We observe that for a given distance d all the correlations feature a similar time evolution: a fast increase followed by a slow decay, with a turning point around 1 μs. For this particular point, the data reveal a plateau for distances of more than six sites—the signature of the LRO mentioned in the main text—that disappears for $t \gtrsim 2$ μs. This suggests that despite the decoherence present in the system, we are able to observe the long-range ordering expected from the dipolar interactions over a substantial time window.

Ground-state properties of the XY model

We study here the ground states of the Hamiltonians H_{XY} and $H_{XY} + H_Z$. We define them as in the main text. First

$$H_{XY} = -\frac{J}{2}\sum_{i<j}\frac{a^3}{r_{ij}^3}[\sigma_i^x\sigma_j^x + \sigma_i^y\sigma_j^y] \tag{4}$$

$$= -\frac{J}{\hbar^2}\sum_{i<j}\frac{a^3}{r_{ij}^3}[S_i^+S_j^- + S_j^+S_i^-] \tag{5}$$

where $S_i^{\pm} = S_i^x \pm iS_i^y = \hbar(\sigma_i^x \pm i\sigma_i^y)/2$ are the ladder operators for spin-1/2 degrees of freedom on a square lattice with N sites, r_{ij} is the distance between sites i and j, and a is the lattice spacing. Second, the on-site Hamiltonian is:

$$H_Z = \hbar\delta\sum_{i\in B}\frac{\sigma_i^z + 1}{2} \tag{6}$$

where the magnitude of the light shift δ depends on the intensity of the addressing laser.

The experimental implementation has an FM coupling, $J/h = 0.77$ MHz, and to study antiferromagnetism one must prepare negative-temperature states. For theoretical purposes, however, we treat J as a free parameter and frame the discussion in terms of the ground-state physics of H_{XY} with either FM ($J > 0$) or AFM ($J < 0$) coupling. We refer to them as H_{XY}^{FM} and H_{XY}^{AFM}.

It is natural to compare the dipolar H_{XY} to the nearest-neighbour XY model on the square lattice,

$$H_{nn} = -\frac{J}{2}\sum_{\langle ij\rangle}\sigma_i^x\sigma_j^x + \sigma_i^y\sigma_j^y, \tag{7}$$

where $\langle ij\rangle$ are pairs of neighbouring sites, with $i < j$. For H_{nn}, the sign of the coupling J is unimportant, as $U_A H_{nn} U_A^\dagger = -H_{nn}$, with $U_A = \prod_{j\in A} e^{-i\pi S_j^z}$. In 1988, Kennedy, Lieb and Shastry rigorously proved that the unique ground state of H_{nn} has long-range XY order[55].

For models with long-range interactions, there are analogous mathematical theorems for classical systems at finite temperature and for quantum systems in which the interaction strength depends on the Manhattan distance $\|r_i - r_j\|_1$ (ref. 19). In a recent work, Björnberg and Ueltschi addressed quantum spin-S models with interactions depending on the Euclidean distance $\|r_i - r_j\|_2$, although their results require a large S and a spatial dimension of three or higher[56]. In the absence of a rigorous proof of LRO for the two-dimensional, spin-1/2, dipolar XY model, we can study it using semi-analytic spin-wave theory and various numerical methods[18,22,27]. In a companion paper (M. Bintz et al., manuscript in preparation), we investigate the ground states of H_{XY} on various geometries, such as tori and infinite cylinders, with an eye towards the thermodynamic limit, $N \to \infty$. Here, we restrict our focus to finite rectangular arrays as probed in the experiment, and use H_{nn} as a reliable benchmark for comparison.

Symmetries, magnetization sectors and order. As emphasized in the main text, H_{XY} possesses the continuous symmetry: $U_z(\theta)H_{XY}U_z(-\theta) = H_{XY}$ with

$$U_z(\theta) = \exp\left(-i\sum_j \theta S_j^z/\hbar\right) = \exp(-i\theta M^z/2) \tag{8}$$

This operator is generated by the total magnetization, $M^z = \sum_i \sigma_i^z$, and represents the Lie group $U(1) \cong SO(2)$. Futhermore, H_{XY} is invariant under the $\mathbb{Z}_2$ Ising symmetry, α_2: $(\sigma^x, \sigma^y, \sigma^z) \to (\sigma^x, -\sigma^y, -\sigma^z)$, as well as any spatial symmetries of the lattice, such as translation or rotation. This model is also time-reversal-symmetric, as represented by the anti-unitary operator $\mathcal{T} = \mathcal{C}$, where $\mathcal{C}$ applies complex conjugation. Here $\mathcal{T}$ differs from the usual $SU(2)$ time-reversal symmetry, which applies the unitary spin rotation $U_y(\pi) = \exp(-i\pi M^y/2)$ in addition to $\mathcal{C}$. Our atypical choice of $\mathcal{T} = \mathcal{C}$ allows it to remain a symmetry in the presence of the on-site perturbation, H_Z.

In a finite, closed quantum system, all eigenstates $|\psi_n\rangle$ of H_{XY} can be chosen to be simultaneous eigenstates of all of these symmetry operators. In particular, they are eigenstates of the total magnetization, $M^z|\psi_n\rangle = \lambda_n^z|\psi_n\rangle$, and so can be collected into magnetization sectors, conventionally labelled by $S^z = M^z/2$. As a consequence, all M^z-non-conserving operators such as σ_i^x and σ_i^y have identically vanishing expectation values, $\langle\sigma_i^x\rangle = \langle\sigma_i^y\rangle = 0$, in any energy eigenstate $|\psi_n\rangle$ or in any superposition of eigenstates within the same magnetization sector.

In the experiment, systematic errors in the measurement process lead to a small, non-zero $\langle\sigma_i^x\rangle \neq 0$. This value is not a consequence of the physics we are interested in. When analysing the experimental data, we thus choose to nullify any single-spin contributions by using the connected correlator,

$$C_{i,j}^x = \langle\sigma_i^x\sigma_j^x\rangle - \langle\sigma_i^x\rangle\langle\sigma_j^x\rangle \tag{9}$$

In the special case of M^z eigenstates with $\langle\sigma^x\rangle = 0$, $C_{i,j}^x = \langle\sigma_i^x\sigma_j^x\rangle$. This correlation function is not generically zero. If $|C_{i,j}^x|$ approaches a constant $C_\infty^x > 0$ for distantly separated spins i, j, then the corresponding state is said to possess long-range XY order or off-diagonal LRO[37]. Such LRO is the defining feature of continuous symmetry breaking in finite quantum systems.

Rather than the long-distance plateau, an equally good order parameter for $U(1)$ symmetry breaking is given by the in-plane magnetization squared

$$m_{FM/AFM}^2 = \frac{1}{N^2}\sum_{i,j}(\pm 1)^{(r_i^x + r_i^y)/a}C_{i,j}^x \tag{10}$$

where a is the lattice spacing, and the sign is taken +1 for m_{FM}^2, and −1 for m_{AFM}^2. In the $N \to \infty$ limit, any state with a correlation plateau $C_\infty^x \neq 0$ will also have a finite magnetization $m_{FM/AFM}^2$ and vice versa[50].

When continuous symmetry breaking occurs in the thermodynamic limit, then at finite size the lowest energy state in each S^z sector will be approximately,

$$|\Gamma_s^{\mathrm{FM/AFM}}\rangle = \frac{1}{\mathcal{N}_s}\int_0^{2\pi}\frac{\mathrm{d}\theta}{2\pi}e^{is\theta}\,|\theta^{\mathrm{FM/AFM}}\rangle \tag{11}$$

where $|\theta^{\mathrm{FM/AFM}}\rangle$ is the classical, symmetry-breaking product state where each spin points at angle θ or $-\theta$ in the xy plane, s is an integer specifying the S^z sector, and $\mathcal{N}_s$ is a normalization factor. Known either as the Anderson tower or Dicke states, $|\Gamma_s\rangle$ are angular momentum eigenstates of an emergent rigid rotor degree of freedom describing the collective orientation of all the spins in the system[48–51]. The true ground states in each S^z sector are also dressed by quantum spin-wave fluctuations, which weaken the magnetic order[48]. For the ideal case of a uniform superposition over fully spin-polarized states $|\theta^{\mathrm{FM/AFM}}\rangle$, the correlations in $|\Gamma_0\rangle$ lead to $C^x_\infty = m^2 = 0.5$, plus $1/N$ corrections. The effective in-plane magnetization of a $U(1)$-symmetric state should thus be identified as $m_{\mathrm{eff}} \equiv \sqrt{2C^x_\infty}$. That is, if one were to add a small symmetry-breaking field, then the corresponding non-symmetric ground state would have an average magnetization $\langle\sigma^x\rangle = m_{\mathrm{eff}}$.

DMRG calculations. For a numerical investigation of the ground states, we apply the DMRG algorithm[46]. We use the general matrix product state (MPS) framework implemented in the TeNPy software library[47]. Whereas MPS are best-representative of one-dimensional quantum systems, it is now routine to apply DMRG to two-dimensional models under certain geometric restrictions[57]. We always work with charge-conserving tensors that respect the $U(1)$ symmetry of the Hamiltonian.

To begin, we use DMRG to compute the ground state of H_{XY} and H_{nn} on $L \times L$ square clusters with open boundary conditions, for $L = 4$, 6, 8 and 10. With all-to-all interactions included, we reliably obtain well-converged states at relatively low MPS bond dimensions, χ, as quantified by the truncation error of the discarded Schmidt states, $\epsilon_{\mathrm{trunc}}$. The most difficult finite system we study is $H_{\mathrm{XY}}^{\mathrm{AFM}}$ on the 10×10 lattice, for which $\epsilon_{\mathrm{trunc}} < 10^{-5}$ at $\chi = 2{,}048$. All other cases achieve the same or better convergence by $\chi = 1{,}024$, or even $\chi < 200$ on the smaller systems.

All DMRG ground states feature the strong $\langle\sigma^x\sigma^x\rangle$ correlations expected in an XY LRO state. In Extended Data Fig. 4, we show the real-space correlation profile $C^x(d)$, which averages $C^x_{i,j} = \langle\sigma^x_i\sigma^x_j\rangle$ over all spins i, j separated by a displacement vector $\mathbf{d}_{ij}$ with length d. The long-range-interacting ferromagnet, $H_{\mathrm{XY}}^{\mathrm{FM}}$, shows a clear plateau in $C^x(d)$ at long distances for all system sizes. Such a plateau is less apparent for $H_{\mathrm{XY}}^{\mathrm{AFM}}$ and H_{nn}, although for either model $C^x(d)$ is still large at the longest distances. Furthermore, $C^x(d)$ increases with L in both models, suggesting the spatial decay of $C^x(d)$ is amplified by finite-size effects.

We also look for a finite squared magnetization, $m^2_{\mathrm{FM/AFM}}$. We plot the finite-size dependence of this quantity in Extended Data Fig. 4b, which is consistent with $m^2_{\mathrm{FM/AFM}} > 0$ as $L \to \infty$. To further test the effects of the long-range interactions, we introduce a cut-off radius R_{max}, and only include interactions between spins i, j separated by distance $d_{ij} < R_{\mathrm{max}}$. We find that ground-state properties converge quickly with respect to this approximation parameter; the long-range interactions do not induce a QPT in either model. In Extended Data Fig. 4c, we show the dependence of $m^2_{\mathrm{FM/AFM}}$ on R_{max}, finding that, at fixed system size, it is not strongly dependent on $R_{\mathrm{max}} > 4$. This is not too surprising: with the moderately fast $1/r^3$ decay, the interaction strength beyond this point is on the order of $0.01J$ or less.

Overall, $H_{\mathrm{XY}}^{\mathrm{FM}}$ is clearly XY LRO, whereas $H_{\mathrm{XY}}^{\mathrm{AFM}}$ and H_{nn} show stronger finite-size effects. Given that H_{nn} is rigorously known to be LRO in the thermodynamic limit, the similar behaviour observed for $H_{\mathrm{XY}}^{\mathrm{AFM}}$ is a strong indication that it is as well.

Quantum phase diagram of $H_{\mathrm{XY}} + H_{\mathrm{Z}}$. We now investigate the ground-state phase diagram in the presence of the externally applied light-shift δ, described by H_{Z} (equation (6)). This perturbation preserves the $U(1)$ symmetry of H_{XY}, as well as the anti-unitary time-reversal symmetry. On the other hand, H_{Z} breaks the Ising symmetry $\sigma^z_i \to -\sigma^z_i$, and reduces the spatial rotation and translation symmetries. For sufficiently large δ, the lowest energy state of $H_{\mathrm{XY}} + H_{\mathrm{Z}}$ has $M^z \neq 0$, but such states are dynamically decoupled from the $S^z = 0$ sector in which the adiabatic preparation protocol takes place. Henceforth, we always consider the ground states within the $S^z = 0$ sector, as these are the ones most relevant to the experiment.

Because the perturbation H_{Z} is $U(1)$ symmetric, the XY LRO phase of H_{XY} may be stable to a sufficiently small staggered field. Microscopically, the dominant effect of a small δ should be to slightly cant the spins towards the z axis. This will in turn modify the spin stiffness and the spin-wave velocity, but not destroy the underlying order. By contrast, when δ is very large, the ground state must be a gapped, trivial paramagnet, in which $\langle\sigma^x\sigma^x\rangle$ correlations decay to zero at long distances[58]. Between these two limits, we expect a QPT at some critical value, δ_{c}, of the applied field. In a companion paper (M. Bintz et al., manuscript in preparation), we investigate this QPT in detail, finding that, in the thermodynamic limit, it is probably a continuous, second-order transition. For $H_{\mathrm{nn}} + H_{\mathrm{Z}}$, the transition is in the three-dimensional XY universality class. For the $1/r^3$ models, the standard theory expectation is that the AFM QPT is in the same universality class as the short-range model (that is, three-dimensional XY), whereas the FM QPT is in a different universality class with mean-field-like critical exponents[15].

Here, we focus our attention on the 6×7 and 10×10 arrays studied in the experiment. We calculate the $S^z = 0$ ground state of $H_{\mathrm{XY}} + H_{\mathrm{Z}}$ at various light shifts δ using DMRG. At these system sizes, the sharp QPT expected in the thermodynamic limit is smoothed to a broad crossover between the XY-ordered phase for small δ and a trivial paramagnet for large δ. Three features of this crossover are shown in Extended Data Fig. 4d–f.

First, in Extended Data Fig. 4d, we plot the staggered σ^z polarization,

$$P_z = \frac{1}{N}\sum_{i\in A}\langle\sigma^z_i\rangle - \frac{1}{N}\sum_{i\in B}\langle\sigma^z_i\rangle \tag{12}$$

which measures the alignment with the staggered field H_Z. For large $\delta \gg \delta_{\mathrm{c}}$, the ground state approaches the staggered product state used to initialize the adiabatic ramp in the experiment, and the polarization saturates to $P_z = 1$. For $\delta = 0$, $P_z = 0$ due to the Ising symmetry of H_{XY}, which enforces $\langle\sigma^z_i\rangle = 0$. We emphasize that $P_z = 0$ is not a generic feature of the XY-ordered phase. Indeed, for small $\delta < \delta_{\mathrm{c}}$, the spins partially align with the applied field, yielding $P_z > 0$.

Extended Data Fig. 4e shows the complementary behaviour for the magnetization, $m^2_{\mathrm{FM/AFM}}$. At small δ, the field-induced canting of the spins towards the z axis causes $m^2_{\mathrm{FM/AFM}}$ to decrease proportionally to δ^2. At large δ, the ground state approaches the (staggered) z-aligned product state, in which $m^2_{\mathrm{FM/AFM}} = 0$. The magnetization changes most rapidly at the crossover, giving rise to the clear peaks in $\mathrm{d}m^2_{\mathrm{FM/AFM}}/\mathrm{d}\delta$ shown in Extended Data Fig. 4f. We take the centre of these peaks as our definition of the crossover point, $\delta_{\mathrm{c}}^{\mathrm{FM/AFM}}$. For the $N = 42$ cluster, the values are $\hbar\delta_{\mathrm{c}}^{\mathrm{FM}}/J = 7.1(3)$, $\hbar\delta_{\mathrm{c}}^{\mathrm{AFM}}/J = 0.8(1)$, and $\hbar\delta_{\mathrm{c}}^{\mathrm{nn}}/J = 2.4(1)$. For the $N = 100$ cluster, we find $\hbar\delta_{\mathrm{c}}^{\mathrm{FM}}/J = 9.5(3)$, $\hbar\delta_{\mathrm{c}}^{\mathrm{AFM}}/J = 0.9(1)$ and $\hbar\delta_{\mathrm{c}}^{\mathrm{nn}}/J = 2.5(9)$. As $N \to \infty$, the smooth crossover is expected to sharpen into a bona fide QPT and $m^2_{\mathrm{FM/AFM}}(\delta)$ will be non-analytic at the critical point.

Adiabatic preparation

We now provide theoretical and numerical analyses of the adiabatic preparation protocol used in the experiment. As mentioned above, we study both the FM and AFM cases considering $H_{\mathrm{XY}}^{\mathrm{AFM}} = -H_{\mathrm{XY}}^{\mathrm{FM}}$. Furthermore, for a time-reversal-symmetric Hamiltonian such as $H = H_{\mathrm{XY}} + H_{\mathrm{Z}}$, the dynamics under $H(t)$ and $-H(t)$ are identical (as long as the initial state is also time-reversal-symmetric)[44]. So for a finite-time (quasi-adiabatic) ramp, the diabatic errors incurred attempting to follow the topmost state of $H_{\mathrm{XY}}^{\mathrm{FM}} + H_{\mathrm{Z}}$ are the same as for a ground-state protocol with $H(t) = H_{\mathrm{XY}}^{\mathrm{AFM}} - H_{\mathrm{Z}}(t)$.

Excitation gaps and an alternative protocol. The success of any finite-duration adiabatic protocol depends crucially on the low-energy spectrum of the system. In particular, as the smallest excitation gap encountered along the chosen path through parameter space decreases, the time required to obtain a final, high-fidelity ground state increases. To this end, we computed the minimal energy gaps, Δ_{min}, using exact diagonalization on finite clusters with periodic boundary conditions.

In Extended Data Fig. 5a, we plot the instantaneous gap Δ_{min} of $H_{\mathrm{XY}}^{\mathrm{FM/AFM}} + H_{\mathrm{Z}}$, in the $S^z = 0$ sector, as a function of the light-shift $\hbar\delta/J$. We expect the gap for either case to be smallest near the QPT (Methods): for the FM, this dip is seen at $\hbar\delta/J \cong 12$, whereas in the AFM the gap is minimal when $\hbar\delta/J \lesssim 2$. The size of the minimal gaps decreases with increasing system size N (darker colours), as one would expect at a QPT. However, we find the minimal finite-size gaps for the FM model are always larger than the ones for the AFM model. This indicates that for the dipolar XY model, the FM requires less total ramp time to prepare than the AFM.

Besides the staggered light-shift ramp demonstrated in the main text, one can conceive a different route for preparing XY-ordered states: tune down a spatially uniform field in the x direction from large values $\hbar\Omega \gg J$ to zero. This is similar to what is done in Rydberg quantum simulations of the two-dimensional Ising model[8,9,59], and was used in a previous experiment to prepare the topological ground state of a one-dimensional XY model[60]. The corresponding Hamiltonian is $H_{\mathrm{XY}}^{\mathrm{AFM(FM)}} + H_{\mathrm{X}}(t)$, with $H_{\mathrm{X}}(t) = \hbar\Omega(t)\sum_i \sigma_i^x/2$. Note that M^z is no longer conserved in the presence of H_{X}.

Extended Data Fig. 5b shows the smallest energy gap for this alternative protocol. The behaviour is very different from the one for the δ sweep discussed above. For FM interactions, the gap does not show any local minimum and remains large until the end of the sweep, where it finally narrows. By contrast, the gap for the XY AFM is small in the whole region $\hbar\Omega/J \lesssim 10$. On the basis of previous studies of the nearest-neighbour XY model[61,62], both of these results are probably a consequence of the expected phase diagram for $H_{\mathrm{XY}}^{\mathrm{FM/AFM}} + H_{\mathrm{X}}$, which we sketch in the inset of Extended Data Fig. 5d. For the XY FM, H_{X} is a relevant perturbation to the ordered phase: any non-zero Ω breaks the $U(1)$ symmetry and, in the thermodynamic limit, immediately destroys the LRO, resulting in a paramagnetic phase. The AFM is also XY-ordered only at the $U(1)$-symmetric point $\Omega = 0$, but a small Ω instead cants the AFM order towards the y direction by a spin-flop process[61,62]. The ground state is then still an antiferromagnet, but one ordered along the y direction, that is, it spontaneously breaks the remaining $\mathbb{Z}_2$ symmetry $\sigma^y \to -\sigma^y$ of $H_{\mathrm{XY}} + H_{\mathrm{X}}$. This canted antiferromagnet (CAF_y) is stable up to a critical value $\hbar\Omega_c/J$ where it finally undergoes a $2+1D$ Ising QPT to the paramagnetic phase[62].

Comparing the gap landscapes in Extended Data Fig. 5a,b suggests that preparing the XY AFM requires less time when using δ sweeps instead of the Ω sweeps. To quantify this, we integrate the squared inverse gaps and define

$$\mathcal{S}_\Delta(\lambda) = \int_{\lambda_0}^{\lambda} \frac{1}{\Delta_{\mathrm{min}}(\lambda')^2}\mathrm{d}\lambda' \tag{13}$$

where $\lambda = \hbar\delta/J$ or $\hbar\Omega/J$ is the dimensionless parameter for either protocol. As one motivation for this quantity, we consider the fidelity susceptibility, χ_{F}, which is the leading term in the expansion of the fidelity $F(\lambda, \lambda+\delta\lambda) = |\langle\psi_0(\lambda)|\psi_0(\lambda+\delta\lambda)\rangle|$ of the ground states $|\psi_0(\lambda)\rangle$ between two close points λ and $\lambda+\delta\lambda$ in parameter space[63],

$$F(\lambda+\delta\lambda) = 1 - \frac{\delta\lambda^2}{2}\chi_{\mathrm{F}} + \ldots \tag{14}$$

The coefficient χ_{F} characterizes how rapidly the ground state changes with λ. For a ramp protocol of the form $H(\lambda) = H_{\mathrm{XY}} + \lambda H_{\mathrm{I}}$, one can show

$$\chi_{\mathrm{F}} = \sum_{n\neq 0} \frac{|\langle\psi_n(\lambda)|H_{\mathrm{I}}|\psi_n(\lambda)\rangle|}{(E_n(\lambda) - E_0(\lambda))^2} \tag{15}$$

where $|\psi_n(\lambda)\rangle$ is the nth eigenstate of $H(\lambda)$ and $E_n(\lambda)$ is the corresponding energy[63]. If we assume that the $n = 1$ term is dominant, and the numerator is nearly constant, we get the relationship $\chi_F \approx 1/(E_1(\lambda) - E_0(\lambda))^2 = 1/\Delta_{\mathrm{min}}(\lambda)^2$. The integral $\mathcal{S}_\Delta$ therefore estimates the total difficulty of adiabatically preparing the ground state of $H(\lambda)$, starting from the ground state of $H(\lambda_0)$.

In Extended Data Fig. 5c,d, we plot $\mathcal{S}_\Delta(\lambda)$ for the two protocols. The initial point λ_0 is taken to be in the paramagnetic phase: $\lambda_0 = 12$ for the δ sweep and $\lambda_0 = 24$ for the Ω sweep. In either case, $\mathcal{S}_\Delta$ for the AFM (blue curve) exceeds that of the FM as $\lambda \to 0$, indicating that the AFM is more difficult to prepare. Most of all, comparing Extended Data Fig. 5c,d one sees that the $H_{\mathrm{Z}}(t)$ protocol is much more efficient at preparing the XY-ordered state ($\lambda = 0$) than the $H_{\mathrm{X}}(t)$ protocol, especially for the AFM.

Time-dependent MPS simulations. To ensure that we have a good understanding of the experiment and its imperfections, we also perform numerical simulations of the full many-body quantum dynamics for the $N = 42$ adiabatic ramp. We simulate the dynamics in the spin-1/2 subspace, taking into account the error tree in Extended Data Fig. 2 by sampling the state preparation errors with $N_{\mathrm{dis}} = 20$ independent simulations.

Atoms that were not excited in the STIRAP with $\eta_{\mathrm{STIRAP}} = 0.03$ correspond to missing sites in the square lattice not taking part in the dynamics. On the remaining sites, we prepare an initial MPS as product state, flipping individual spins according to the probabilities of the microwave π pulse, $\eta_{\mathrm{MW}} = 0.003$, and the subsequent microwave sweep of the addressed atoms, $\eta_{\mathrm{A}} = 0.10$, $\eta_{\mathrm{B}} = 0.03$. These values are slightly different from those reported in Extended Data Table 1, reflecting an earlier calibration of the experiment. We further update the atom distances r_{ij} in H_{XY} to account for positional disorder: we first take a normal-distributed initial displacement from the square lattice with variance $\sigma_r = 0.2$ μm, followed by a movement during the dynamics with normal-distributed (time-independent) velocity of variance $\sigma_v = 0.05$ μm μs^{-1} corresponding to the temperature of the atoms.

We then time-evolve the states under the time-dependent Hamiltonian,

$$H(t) = -J\sum_{i<j}\frac{a^3}{r_{ij}^3(t)}[S_i^+S_j^- + S_i^-S_j^+] + H_{\mathrm{vdW}} + \delta(t)\epsilon_{\mathrm{AFM}}\sum_{i\in B}\frac{1+\sigma_i^z}{2} \tag{16}$$

where $J/h = 0.77$ MHz, $\delta(t)$ is the ramp shown in Extended Data Fig. 6a,c (insets) and $\epsilon_{\mathrm{AFM}} = -1$ for the antiferromagnet (+1 for the ferromagnet). The extra term, H_{vdW}, accounts for the van der Waals interactions between the Rydberg atoms, and takes the form

$$H_{\mathrm{vdW}} = \sum_{i<j}\frac{a^6}{r_{ij}^6(t)}[U_6^{PP}P_i^\uparrow P_j^\uparrow + U_6^{SS}P_i^\downarrow P_j^\downarrow + U_6^{SP}(P_i^\uparrow P_j^\downarrow + P_i^\downarrow P_j^\uparrow)] \tag{17}$$

where $P_i^{\uparrow/\downarrow} = S_i^z \pm 1/2$ are single-spin projectors. The values of the U_6 coefficients are $U_6^{PP}/h = -0.008$, $U_6^{SS}/h = 0.037$ and $U_6^{SP}/h = -0.0007$ MHz. For the purposes of this simulation, we restrict the interaction range of H_{XY} and H_{vdW} to $R_{\mathrm{max}} < 3.7$. We use the W_{II} method[64] to approximate the evolution operator $\mathrm{e}^{-i(H/\hbar)\mathrm{d}t}$ as a matrix product operator (MPO), in combination with standard variational MPO-MPS compression methods. Our scheme is correct to first order in the time step $\mathrm{d}t = 0.01$ μs$/2\pi$. As the evolution is sufficiently adiabatic, a moderate bond dimension of $\chi = 128$ is enough to capture the correlations. In the DMRG ground state, the truncation error at this bond dimension is 6×10^{-7} for the ferromagnet, and 3×10^{-5} for the antiferromagnet.

When evaluating expectation values and correlation functions from the time-evolved MPS (t-MPS), we further account for the measurement

errors $\eta_{frz} = 0.01$, $\eta_{dx} = 0.03$, $\epsilon = 0.01$, $\epsilon' = 0.07$ of the error tree. This can be done exactly (without another sampling procedure), because the MPS gives full access to the probabilities of the individual measurement outcomes.

There are two notable experimental imperfections that we do not take into account in these simulations. First, there are further sources of decoherence in the experiment as discussed in Decoherence during the adiabatic ramp. Second, in our numerical simulations, we assume that all errors in the error tree occur independently for each atom and result in an initial product state of up or down spins or vacant holes. Yet, the STIRAP and microwave pulses leave the atoms in coherent superpositions of the relevant atom levels.

Simulation results for $N = 42$. The results of the t-MPS simulations are shown in Extended Data Fig. 6, which also includes direct comparisons to the experimental measurements, and to the DMRG ground state. For our ensemble of $N_{dis} = 20$ independent t-MPS simulations, we show the average values of these simulations with solid lines, whereas the shaded region indicates the standard deviation.

Our first observable (Extended Data Fig. 6a,c) is the staggered polarization $P_z = \sum_{A,B} (\pm) \langle \sigma_i^z \rangle$. For the antiferromagnet, the agreement between the t-MPS simulations and experiment is essentially perfect for all values of δ. This is a strong indication that most dominant sources of error in the experiment have been accurately accounted for. For the ferromagnet, there is a small offset between the t-MPS calculation and the experimental result at late times (small δ). In particular, $P_z \to 0$ as $\delta \to 0$ for the t-MPS calculation, whereas $P_z \to -0.06$ in the experiment. This discrepancy is due to the sublattice-dependent depumping from the light shift discussed in Decoherence during the adiabatic ramp, which we do not account for in the t-MPS simulations.

As the state loses its initial σ^z polarization, it concomitantly develops XY order. This is tracked by the order parameter m^2_{FM} (m^2_{AFM} for the antiferromagnet), shown in Extended Data Fig. 6b,d. We obtain again a good agreement between the t-MPS simulation and the experiment at early times (large δ), although we caution that the initial positive value of $m^2_{FM/AFM} = 1/42$ is inherent to any σ_i^z-product state. On top of the smooth adiabatic envelope, the t-MPS simulations reveal coherent oscillations in P^z and $m^2_{FM/AFM}$. These oscillations are a feature of the large-δ paramagnetic phase, and are essentially Rabi oscillations between the classical Néel ground state and the 42-fold degenerate manifold of states with one spin-flip excitation.

At small δ, the experimental measurements of $m^2_{FM/AFM}$ fall below the t-MPS predictions. This deficit probably arises from a combination of decoherence and unmodeled systematic errors, such as experimental imperfections in the $\pi/2$-pulse rotation to the x basis. Regarding the latter, an imperfect basis rotation means that the operator measured in the experiment is not exactly σ_i^x but some small modification of it, $\tilde{\sigma}_i^x = U \sigma_i^x U^\dagger$. In XY-ordered states, $\langle \sigma^x \sigma^x \rangle = \langle \sigma^y \sigma^y \rangle$ correlations are typically much larger than any other two-body operators, especially at long distances. Measuring any modified $\tilde{\sigma}_i^x$ will then generically reduce the value of the inferred magnetization, $\tilde{m}^2_{FM} = 2 \sum_{i,j} \langle \tilde{\sigma}_i^x \tilde{\sigma}_j^x \rangle$.

We also use the t-MPS simulation to assess the quality of the adiabatic preparation. In particular, we are interested in how close the unitary dynamics comes to preparing the target ground state of H_{XY}. We measure this by means of the XY energy $E_{XY} = \langle H_{XY} \rangle$, which corresponds to the amount of energy the many-body state stores within the dipolar interaction. The ideal endpoint of the ramp is a state that maximizes $|E_{XY}|$, that is, the ground state of H_{XY} (or, the topmost state in the case of the negative-temperature preparation for the antiferromagnet). We do not include measurement errors for this analysis, as we want to directly compare the adiabatically prepared state to the ideal one. As a minor technical point, the ensemble of lattices used in the t-MPS simulation occasionally have missing sites (representing an absence of Rydberg-excited atoms), and always have some position disorder that modifies the couplings, Ja^3/r_{ij}^3, and hence the spectrum of H_{XY}. To treat the different lattices on even footing, when measuring E_{XY} we compute the expectation value of H_{XY} without position disorder in the couplings, and normalize by the total number of active sites, $\bar{N}$, before taking the ensemble average.

Extended Data Fig. 7a,b shows $E_{XY}(\delta)/J\bar{N}$ in the DMRG ground state (purple), the ensemble-averaged t-MPS simulation (teal) and a single state within the t-MPS ensemble (pink) that had a nearly perfect initial configuration: one missing site at the corner, and all remaining spins properly aligned with the staggered field. Initially, the system is in a classical ensemble of σ_i^z-aligned product states, so $E_{XY}(t = 0) = 0$. The dynamics generated by $H(t)$ produce the desired correlations among the spins; the oscillations in E_{XY} at large δ are the paramagnetic Rabi oscillations also observed in P_z and m_x^2. At the end of the ramp, the ensemble averages are $E^{FM}_{XY}/(\bar{N}J) = -1.41(8)$ and $E^{AFM}_{XY}/(\bar{N}J) = -0.64(3)$, which correspond to 94 ± 5 and $89 \pm 4\%$ of the $N = 42$ ground-state value, respectively. The near-ideal initial state produces a near-ideal final state, achieving 99.7% (FM) and 98.2% (AFM) of the ground-state energy density. This indicates that any diabatic errors during the ramp are negligible compared to the initialization errors.

As discussed in Excitation gaps and an alternative protocol, the quality of a finite-time adiabatic ramp crucially depends on the size of the many-body energy gap. For the $U(1)$-symmetric ramp at hand, the quantity is the (spin-)neutral gap, $\Delta_0 = E_1(S^z = 0) - E_0(S^z = 0)$. In the paramagnetic phase, $\Delta_0 \cong \delta$, whereas in the XY-ordered phase one expects $\Delta_0^{FM} \propto 1/\sqrt{N}$ and $\Delta_0^{AFM} \propto 1/N$ (refs. 18,27). The numerical value of Δ_0 on finite-size systems can be computed in DMRG by solving for the lowest energy state orthogonal to the previously obtained ground state, in the same $S^z = 0$ sector. We plot $\Delta_0(\delta)$ in Extended Data Fig. 7c,d for both the $N = 42$ and $N = 100$ clusters. The behaviour of $\Delta_0(\delta)$ differs from that seen in Excitation gaps and an alternative protocol, due to a difference in boundary conditions (open instead of periodic). Across the phase diagram, $\Delta_0(\delta)$ is fairly large, which helps to explain the success of the adiabatic preparation: the ramp decay time scale, $\tau = 1.45\,\hbar/J$, is slower than (FM) or approximately equal to (AFM) the inverse gap, $\Delta_0^{-1} = 0.45/J$ (FM), $1.47/J$ (AFM). The smaller gap for the antiferromagnet is a manifestation of its frustration, and makes adiabatically preparing its ground state more difficult compared to H^{FM}_{XY}. Comparing Δ_0 to the excess energy the end of the ramp, we find that the near-ideal initial state ends up with a total effective energy, $\mathcal{E} = NE_{XY}/\bar{N}$, below the many-body gap. The difference is large for the ferromagnet ($\mathcal{E}/\Delta_0^{FM} = 0.06$), indicating a near-flawless adiabatic sweep, whereas the margin for the antiferromagnet is much narrower ($\mathcal{E}/\Delta_0^{AFM} = 0.81$).

Thermal phase diagram

We conclude by discussing the phase diagram of $H_{XY} + H_Z$ at finite temperature, T (measured in unit of k_B). Whereas two-dimensional, $U(1)$-symmetric systems can have XY LRO ground states, for short-range interacting models such as H_{nn} this order does not persist to finite temperature[12,13,65,66]. Physically, this is because spin-wave excitations (that is, Goldstone modes) proliferate at finite temperature and destroy the XY order. Instead, most two-dimensional XY models have an algebraic long-range ordered phase at low temperatures, separated from the high-T disordered phase by a BKT transition at a critical temperature T_{BKT} (refs. 38–41). The low-T phase is characterized by power-law-decaying correlations, $C^x(d) \cong d^{-1/(2\pi K)}$, with a temperature-dependent exponent K that attains the universal value $K_{BKT} = 2/\pi$ at T_{BKT}. For the classical nearest-neighbour XY model, $T^{cl}_{BKT}/(2J) = 0.892943(2)$ (refs. 67,68), whereas in the quantum spin-1/2 H_{nn} the transition is lowered to $T^{nn}_{BKT}/(2J) = 0.353(3)$ (refs. 69,70).

Long-range FM interactions can suppress the proliferation of spin waves and thus renew the possibility for XY LRO at finite temperature[18,19,27]. With $1/r^\alpha$ FM couplings, extensively large fluctuations of the spin orientation come at an energy cost proportional to $L^{4-\alpha}$, with L the linear system size, so two-dimensional XY LRO can be thermodynamically stable when $\alpha \leq 4$. Indeed, in 1976, Kunz and Pfister proved that

the classical version of H_{XY}^{FM} shows a finite-temperature phase transition between the high-T disordered phase and a low-T XY LRO phase[17]. Subsequent Monte Carlo simulations located this transition at $T_c^{FM}/(2J) = 3.96(4)$, and suggested it was weakly first order[71,72]. We note this is contrary to the general expectation of a second-order symmetry-breaking transition, in a mean-field-like universality class when $\alpha \leq 3$ (refs. 15,73,74). Finally, $1/r^{\alpha}$ AFM interactions do not essentially modify the energy of long-wavelength fluctuations, so one expects the low-T physics of H_{XY}^{AFM} to be similar to that of H_{nn} (ref. 14).

Numerical phase diagram for $N = 42$. For a quantitative understanding of the thermal physics accessible in the experiment, we numerically investigate the finite-temperature phase diagram for both the FM and the AFM on the 6×7 lattice. Whereas H_{XY}^{FM} is amenable to quantum Monte Carlo techniques, these are not an option for H_{XY}^{AFM}, which shows a sign problem. Instead, for both we use the minimally entangled typical thermal states (METTS) algorithm[75]. This is a Markov chain Monte Carlo approach that alternates between evolving a state in imaginary time to inverse temperature $\beta/2$, and then taking a projective measurement as the initialization for the next imaginary time evolution. The result is an ensemble of pure states, $\{|\psi_{METTS}\rangle\}$, that approximates the thermal density matrix $\rho \propto e^{-\beta H}$: for any operator $\mathcal{O}$, the ensemble average of $\langle\psi_{METTS}|\mathcal{O}|\psi_{METTS}\rangle$ approaches the thermal equilibrium value $\mathrm{Tr}[\rho\mathcal{O}]$.

Owing to the $U(1)$ symmetry, the thermal density matrix factorizes into a direct sum over the different magnetization sectors, $\rho = \bigoplus_{m=-N}^{N} \rho_m$. Here, we sample only from the $m = 0$ sector, as this is the most relevant one for the partial quench experiment. For numerical convenience, we also truncate the long-range interactions to $R_{max} < 3.7$, and omit the van der Waals coupling, position disorder, and the possibility of holes. We perform the imaginary time evolution using the same W_{II} MPO-MPS method as in Simulation results for $N = 42$, taking an MPS bond dimension of $\chi = 256$. We found very similar results using $\chi = 128$ (not shown), albeit with some small quantitative shifts near the finite-temperature phase transition. To reduce sample autocorrelations, each projective measurement is made in a random basis determined by a depth-two, $U(1)$-conserving random unitary circuit[76]. By a standard blocking analysis, we estimate the resulting autocorrelation time to be about ten Markov chain Monte Carlo steps[77]. We therefore allow a warm-up time of 20 steps, and then generate 100–300 samples for each value of δ and β.

In Extended Data Fig. 8a,f, we show two-dimensional colour plots of the squared magnetization $m_{FM/AFM}^2$ at finite T and δ. For the ferromagnet (Extended Data Fig. 8a), we observe a lobe around $(T, \delta) = (0, 0)$ that corresponds to the XY-ordered phase. The order begins to disappear around $T/J = 1.5$ (for the thermal phase transition) and $\delta/J = 5$ (for the QPT). Examining m_{AFM}^2 for the AFM case (Extended Data Fig. 8b), we observe a smaller lobe with apparent XY order. Although H_{XY}^{AFM} is not predicted to host true LRO at $T > 0$, obtaining $m_{AFM}^2 > 0$ is still possible on finite-size systems.

Owing to the small system size, there is a smooth crossover between the ordered and disordered regimes for both models, and it is difficult to ascertain what the nature of the phase transition may be in the thermodynamic limit. It should be possible to study larger system sizes for H_{XY}^{FM} using Quantum Monte Carlo methods[78], which is beyond the scope of this work. For now, we cautiously estimate $T_{XY}^{FM}/J \approx 1.5$ and $T_{XY}^{AFM}/J \approx 0.5$, as the $\delta = 0$ crossover temperature into the high-T phase. Compared to H_{nn}, for which $T_{BKT}^{nn}/J = 0.706(6)$ (refs. 69,70), the dipolar ferromagnet seems to have a higher transition temperature (although not as high as the classical model[71,72]), whereas the antiferromagnet may have a slightly lower one.

Temperature estimate of the final state. With our minimally entangled typical thermal states representation of the thermal density matrix, we also determine the temperature and δ dependence of the internal energy, $E(T) = \mathrm{Tr}[\rho H]$. The inverse function $T(E)$ defines a temperature calibration: we estimate the effective temperature of a state from its energy density. Inputting the mean final energy density of our t-MPS simulations (Adiabatic preparation—theory and numerics), we estimate the effective temperatures at the end of the adiabatic ramp to be $T_{MPS}^{FM}/J = 0.95$ and $T_{MPS}^{AFM}/J = 0.53$. The t-MPS disorder ensemble results in a spread of energies $E_{XY} \pm \sigma_E$; the corresponding temperature intervals are $T_{MPS}^{FM} \in [0.46, 1.17]$ and $T_{MPS}^{AFM} \in [0.45, 0.60]$. These intervals are asymmetric about the mean value due to the non-linearity of $T(E)$. The obtained T_{MPS}^{FM} seems to be below the estimated crossover temperature T_{XY}^{FM}, whereas for the antiferromagnet T_{MPS}^{AFM} is very close to the phase transition. This is consistent with the wide spread in magnetizations m_{AFM}^2 over the t-MPS ensemble, shown in Extended Data Fig. 6d.

Temperature calibration of quantum quenches. Performing an analogous $T(E)$ calibration at finite δ, we also estimate the effective temperatures produced by the quantum quench experiments (Fig. 1c,e,f), with final light-shift δ_f and quench magnitude δ_q. We assume that, following the quench, the system equilibrates to a thermal state; extensively testing this assumption with numerical quench simulations is challenging, but may be interesting to explore in the future. Barring the possibility of a non-thermal equilibrium, our basic expectation is that the quench affects the XY order by a mechanism not unlike a finite-temperature bath. In particular, the excess energy added into the system should excite the low-energy, symmetry-restoring spin waves[79]. If the resulting population density of spin waves at equilibrium is not too different from a true thermal distribution, then in the thermodynamic limit it will destabilize the XY AFM order but not the XY FM order at low temperature.

We first calculate the effective temperature assuming perfect adiabatic preparation up to the prequench point $\delta_f + \delta_q$, that is, by evaluating the energy $\langle H_{XY} + H_Z(\delta_f)\rangle$ in the DMRG ground state of $H_{XY} + H_Z(\delta_f + \delta_q)$ and then converting it to a temperature. Extended Data 8b,g shows the effective temperature $T_{eff}(\delta_f, \delta_q)/J$ for the FM and the AFM. In the FM, modest quenches $\delta_q/2\pi < 4$ MHz uniformly increase the effective temperature as a function of δ_f over the range $\delta_f/2\pi \in [0, 3.5]$ MHz probed in the experiment. With larger quenches, the effective temperature increases rapidly for small values of δ_f and slows down at larger values of δ_f. In the AFM, the effective temperature produced by even small quenches δ_q has a strong dependence on δ_f, again being much more effective at raising the temperature as $\delta_f \to 0$ (that is, the isotherms are steeply sloped at small δ_f). Extended Data Fig. 8d,i shows the corresponding magnetization $m_{FM/AFM}^2$ expected at $T_{eff}(\delta_f, \delta_q)$. Notably, in the AFM the large variation in $T_{eff}(\delta_f)$ at a fixed δ_q leads to a 'tilted Matterhorn' shape for the ordered region.

Finally, we estimate the effective temperature of the full experimental protocol by using the states produced in the t-MPS ramp simulation as the prequench configuration. We show $T_{eff}(\delta_f, \delta_q)/J$ for the FM and AFM in Extended Data Fig. 8c,h. As a consequence of the paramagnetic Rabi oscillations discussed previously in Simulation results for $N = 42$, T_{eff} is also oscillatory. For the FM, these oscillations only manifest at large δ_q (corresponding to prequench states taken very early in the ramp), whereas for the AFM they are relevant across the phase diagram. The latter behaviour ultimately stems from the fact that $\delta_c^{AFM}/2\pi \approx 0.7$ MHz, so most prequench states are in the paramagnetic phase.

The corresponding magnetization $m_{FM/AFM}^2(T_{eff})$ is shown in Extended Data Fig. 8e,j. Comparing to the experimental results in Fig. 1e,f, we see that some qualitative features are reproduced by this calculation, especially for the AFM. For instance, the sloped phased boundary seen in the experiment at small δ_f is due to the diagonal isotherms. The calculation seems to differ from the experiment in the region with large δ_f (that is, $\delta_f/2\pi > 2(1)$ MHz for the FM (AFM)) and small δ_q. In particular, the order–disorder crossover seems to happen at larger δ_f than seen in the experiment, and the observed non-monotonic behaviour of $m_{FM/AFM}^2(\delta_q)$ is also less apparent. These differences may come from the same unmodeled imperfections that led to a discrepancy in the absence of any quench (Simulation results for $N = 42$). Another

possibility is that the thermal density matrix $\rho(T_{\mathrm{eff}})$ in the $M^z = 0$ sector may be an inadequate approximation of the post-quench state, either due to non-thermal equilibration or neglected contributions from different magnetization sectors.

Data availability

The data are available from the corresponding author on reasonable request.

53. Barredo, D., de Léséleuc, S., Lienhard, V., Lahaye, T. & Browaeys, A. An atom-by-atom assembler of defect-free arbitrary 2D atomic arrays. *Science* **354**, 1021–1023 (2016).
54. de Léséleuc, S., Barredo, D., Lienhard, V., Browaeys, A. & Lahaye, T. Analysis of imperfections in the coherent optical excitation of single atoms to Rydberg states. *Phys. Rev. A* **97**, 053803 (2018).
55. Kennedy, T., Lieb, E. H. & Shastry, B. S. in *Statistical Mechanics* (eds Nachtergaele, B. et al.) 327–329 (Springer, 1988).
56. Björnberg, J. E. & Ueltschi, D. Reflection positivity and infrared bounds for quantum spin systems. In *The Physics and Mathematics of Elliott Lieb* 77–108 (EMS Press, 2022).
57. Stoudenmire, E. & White, S. R. Studying two-dimensional systems with the density matrix renormalization group. *Ann. Rev. Condens. Matter Phys.* **3**, 111–128 (2012).
58. Hastings, M. B. & Koma, T. Spectral gap and exponential decay of correlations. *Commun. Math. Phys.* **265**, 781–804 (2006).
59. Lienhard, V. et al. Observing the space- and time-dependent growth of correlations in dynamically tuned synthetic Ising antiferromagnets. *Phys. Rev. X* **8**, 021070 (2018).
60. de Léséleuc, S. et al. Observation of a symmetry-protected topological phase of interacting bosons with Rydberg atoms. *Science* **365**, 775–780 (2019).
61. Jensen, P. J., Bennemann, K. H., Morr, D. K. & Dreyssé, H. Two-dimensional Heisenberg antiferromagnet in a transverse field. *Phys. Rev. B* **73**, 144405 (2006).
62. Kar, S., Wierschem, K. & Sengupta, P. Magnons in a two-dimensional transverse-field XXZ model. *Phys. Rev. B* **96**, 045126 (2017).
63. Gu, S.-J. Fidelity approach to quantum phase transitions. *Int. J. Mod. Phys. B* **24**, 4371–4458 (2010).
64. Zaletel, M. P., Mong, R. S. K., Karrasch, C., Moore, J. E. & Pollmann, F. Time-evolving a matrix product state with long-ranged interactions. *Phys. Rev. B* **91**, 165112 (2015).
65. Mermin, N. D. Crystalline order in two dimensions. *Phys. Rev.* **176**, 250–254 (1968).
66. Fröhlich, J. & Pfister, C. On the absence of spontaneous symmetry breaking and of crystalline ordering in two-dimensional systems. *Commun. Math. Phys.* **81**, 277–298 (1981).
67. Tobochnik, J. & Chester, G. V. Monte Carlo study of the planar spin model. *Phys. Rev. B* **20**, 3761–3769 (1979).
68. Ueda, A. & Oshikawa, M. Resolving the Berezinskii-Kosterlitz-Thouless transition in the two-dimensional XY model with tensor-network-based level spectroscopy. *Phys. Rev. B* **104**, 165132 (2021).
69. Ding, H.-Q. & Makivić, M. S. Kosterlitz-Thouless transition in the two-dimensional quantum XY model. *Phys. Rev. B* **42**, 6827–6830 (1990).
70. Ding, H.-Q. Phase transition and thermodynamics of quantum XY model in two dimensions. *Phys. Rev. B* **45**, 230–242 (1992).
71. Romano, S. Computer simulation study of a long-range plane-rotator system in two dimensions. *Nuovo Cim, B* **100**, 447–466 (1987).
72. Romano, S. Computer-simulation study of a disordered plane-rotator system in two dimensions with long-range ferromagnetic interactions. *Phys. Rev. B* **42**, 8647–8650 (1990).
73. Fisher, M. E., Ma, S.-k & Nickel, B. G. Critical exponents for long-range interactions. *Phys. Rev. Lett.* **29**, 917–920 (1972).
74. Sak, J. Recursion relations and fixed points for ferromagnets with long-range interactions. *Phys. Rev. B* **8**, 281–285 (1973).
75. Stoudenmire, E. M. & White, S. R. Minimally entangled typical thermal state algorithms. *New J. Phys.* **12**, 055026 (2010).
76. Binder, M. & Barthel, T. Symmetric minimally entangled typical thermal states for canonical and grand-canonical ensembles. *Phys. Rev. B* **95**, 195148 (2017).
77. Gubernatis, J., Kawashima, N. & Werner, P. *Quantum Monte Carlo Methods: Algorithms for Lattice Models* 1st edn (Cambridge Univ. Press, 2016).
78. Syljuasen, O. F. & Sandvik, A. W. Quantum Monte Carlo with directed loops. *Phys. Rev. E* **66**, 046701 (2002).
79. Calabrese, P. & Cardy, J. Time dependence of correlation functions following a quantum quench. *Phys. Rev. Lett.* **96**, 136801 (2006).

Acknowledgements We acknowledge the insights of and discussions with M. Aidelsburger, L. Henriet, V. Lienhard, J. Moore, C. Laumann, B. Halperin, E. Altman, B. Ye, E. Davis and M. Block. We are especially indebted to H.P. Büchler for insightful comments and discussions about the role of dipolar interactions in the XY model. The computational results presented were performed in part using the FASRC Cannon cluster supported by the FAS Division of Science Research Computing Group at Harvard University, the Savio computational cluster resource provided by the Berkeley Research Computing programme at the University of California, Berkeley and the Vienna Scientific Cluster. This work is supported by the European Union's Horizon 2020 research and innovation programme under grant agreement no. 817482 (PASQuanS), the Agence Nationale de la Recherche (ANR, project nos. RYBOTIN and ANR-22-PETQ-0004, project QuBitAF) and the European Research Council (advanced grant no. 101018511-ATARAXIA). J.H. acknowledges support from the NSF OIA Convergence Accelerator programme under award number 2040549, and the Munich Quantum Valley, which is supported by the Bavarian state government with funds from the Hightech Agenda Bayern Plus. M.S. and A.M.L. acknowledge support by the Austrian Science Fund (FWF) through grant no. I 4548. D.B. acknowledges support from grant no. MCIN/AEI/10.13039/501100011033 (grant nos. RYC2018- 025348-I, PID2020-119667GA-I00 and European Union NextGenerationEU PRTR-C17.I1). M.P.Z. acknowledges support from the Department of the Environment (DOE) Early Career programme and the Alfred P. Sloan foundation. N.Y.Y. acknowledges support from the Army Research Office (ARO) (grant no. W911NF-21-1-0262), the AFOSR MURI programme (grant no. W911NF-20-1-0136), the David and Lucile Packard foundation, and the Alfred P. Sloan foundation. M.B. and V.L. acknowledge support from NSF QLCI programme (grant no. OMA-2016245). S.C. acknowledges support from the ARO through the MURI programme (grant no. W911NF-17-1-0323) and from the US DOE, Office of Science, Office of Advanced Scientific Computing Research, under the Accelerated Research in Quantum Computing programme.

Author contributions C.C., G.B., M.B. and G.E. contributed equally to this work. C.C., G.B., G.E., P.S. and D.B. carried out the experiments. M.B., L.L., V.S.L., J.H., S.C. and M.S. conducted the theoretical analysis and simulations. A.M.L., M.P.Z., T.L., N.Y.Y. and A.B. supervised the work. All authors contributed to the data analysis, progression of the project and on both the experimental and theoretical side. All authors contributed to the writing of the manuscript.

Competing interests A.B. and T.L. are cofounders and shareholders of PASQAL. The remaining authors declare no competing interests.

Additional information

Correspondence and requests for materials should be addressed to Antoine Browaeys.

Peer review information *Nature* thanks the anonymous reviewers for their contribution to the peer review of this work.

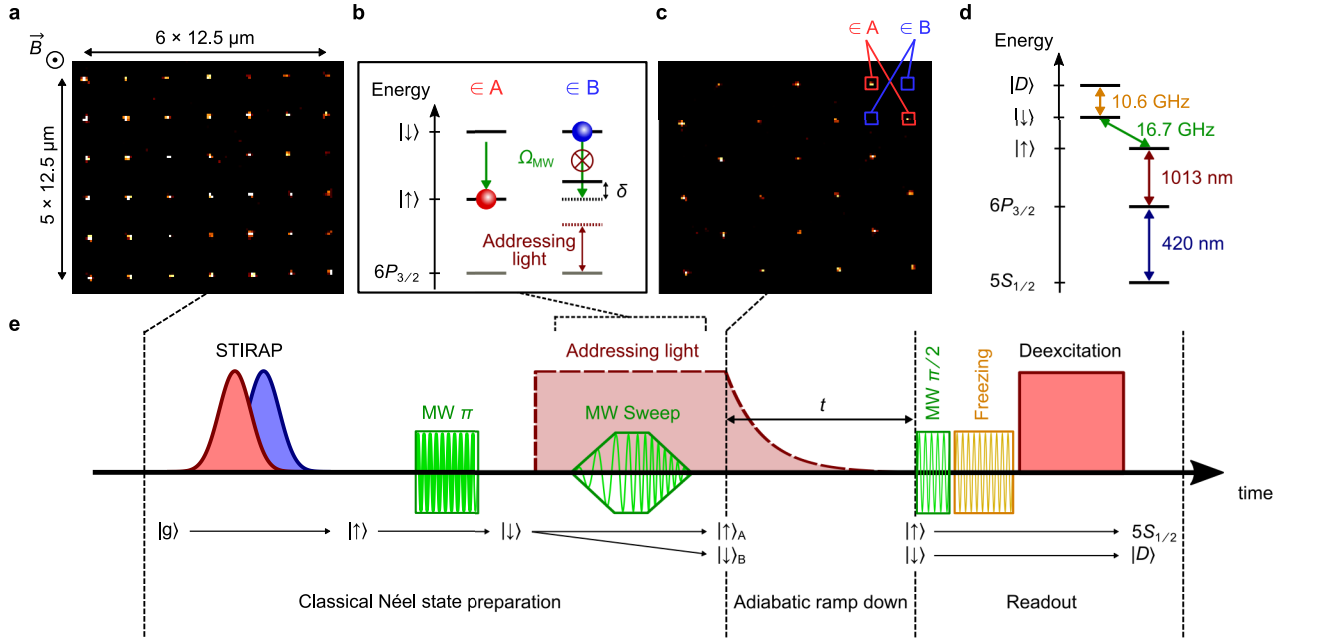

Extended Data Fig. 1 | Experimental procedures and sequence. a, Fluorescence image of the atoms in a fully assembled 6 × 7 array. **b**, Scheme for the preparation of the initial staggered state. **c**, Detected staggered state, corresponding to the situation for which all the atoms in sublattice A are in $|\uparrow\rangle$, and all the atoms in sublattice B are in $|\downarrow\rangle$. **d**, Schematics of the atomic level diagram. **e**, Experimental sequence.

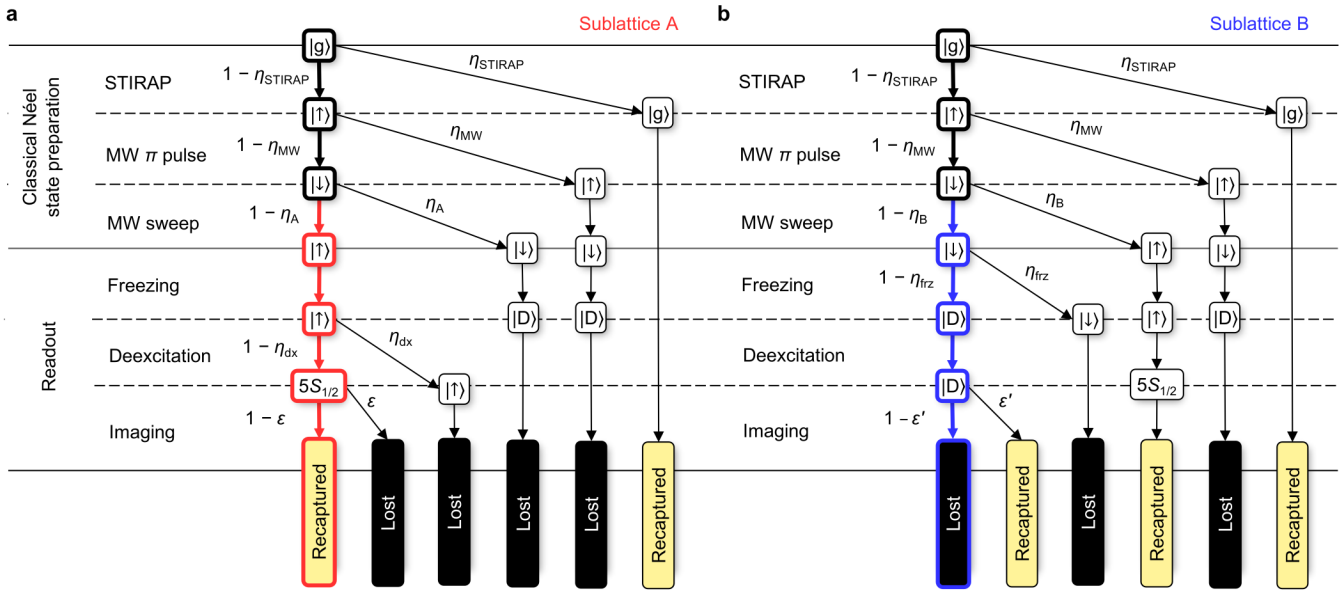

Extended Data Fig. 2 | Simplified error tree associated to the preparation of the initial Néel state, for a the atoms in sublattice A (non-addressed), and b in sublattice B (addressed). For simplicity, the events with a probability of order 2 or higher in the $\eta_i, \epsilon, \epsilon'$ are disregarded.

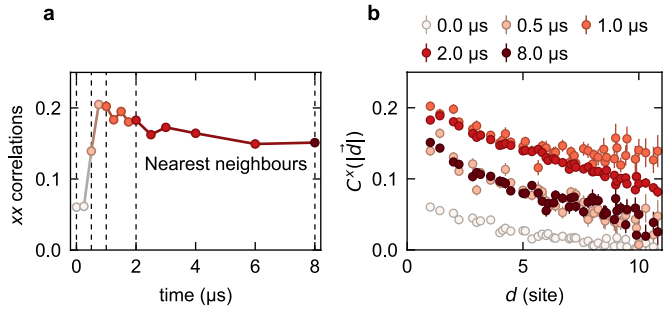

Extended Data Fig. 3 | Time dependence of the correlations along *x* in the FM case for a 10 × 10 lattice. a, Time evolution of the nearest-neighbour correlations along *x* (different colors correspond to different times). **b**, Spatial correlations as a function of distance, measured at different times $t = \{0.0, 0.5, 1.0, 2.0, 8.0\}\,\mu$s indicated by dashed lines in **a**.

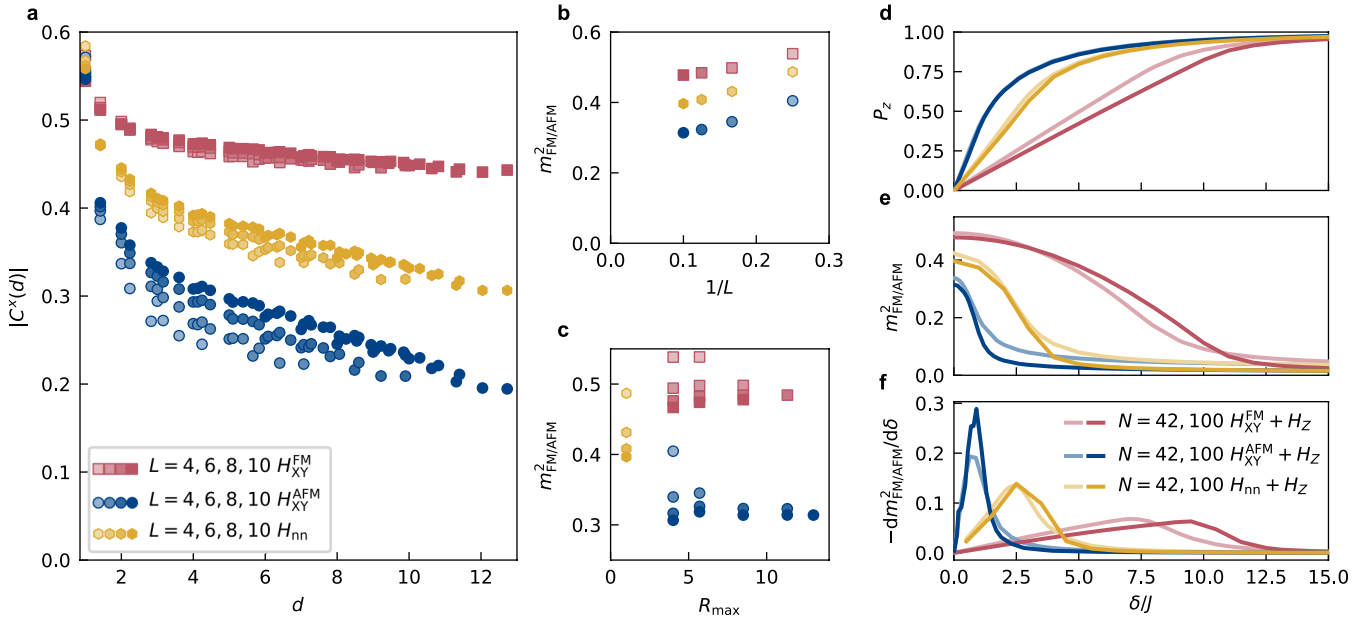

Extended Data Fig. 4 | DMRG ground state calculations. a, Real-space correlation profile $|C^x(d)|$ on $L \times L$ square clusters with open boundary conditions. The ground state of H_{XY}^{FM} clearly exhibits XY LRO at all system sizes. For H_{XY}^{AFM} and H_{nn}, the correlations decrease at long distances, but this decay is reduced as L increases. **b**, Finite-size scaling of the magnetization $m^2_{FM/AFM}$. All three models are consistent with $m^2_{FM/AFM} > 0$ as $L \to \infty$. **c**, Dependence of $m^2_{FM/AFM}$ on the interaction distance cutoff R_{max}. At each system size, the ground state correlations are well-converged by $R_{max} \simeq 4$. **d**–**f**, Ground state properties of $H_{XY} + H_Z$ as a function of δ. There is a smooth crossover from the XY ordered state at $\delta = 0$ to the staggered paramagnet as $\delta \to \infty$. The $-dm^2/d\delta$ peaks (**f**) are finite-size incarnations of the quantum phase transition expected in the thermodynamic limit; we use their centers to define the crossover point $\hbar\delta_c/J$.

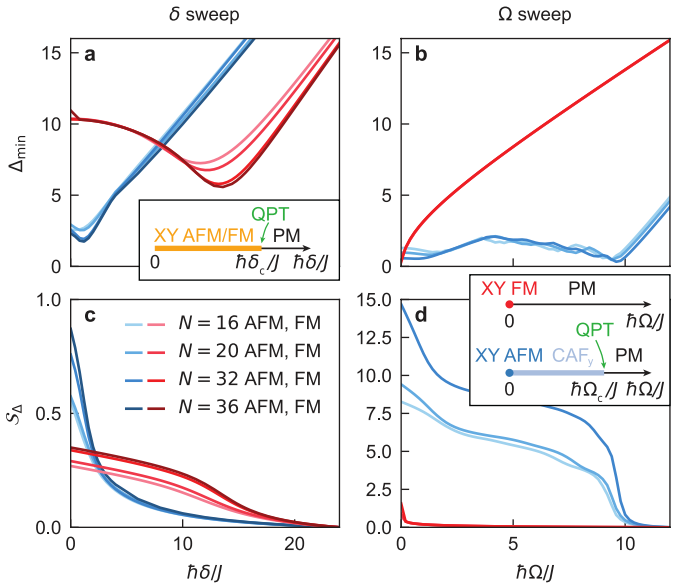

Extended Data Fig. 5 | Excitation gap for two adiabatic preparation protocols. a, Minimal energy gaps of $H_{XY}^{AFM(FM)} + H_Z$ to the lowest excited state in the $M^z = 0$ sector as a function of $\hbar\delta/J$. We here only consider gaps among states with momentum $\mathbf{k} = 0$ and fully symmetric under the lattice point-group, which reflects the setup in the (ideal) experiment. Blue (red) curves show the results for the AFM (FM) model. Darker colors correspond to larger system sizes. The inset shows a sketch of the expected phase diagram. **b**, Same as **a**, but for the protocol with Hamiltonian $H_{XY}^{AFM(FM)} + H_X$. Here we cannot restrict the analysis to a single M^z sector since it is not conserved. **c**, Cumulatively integrated $1/\Delta_{min}^2$ [starting from the largest value $\hbar\delta/J = 24$] for the gaps shown in **a**. The values at $\hbar\delta/J = 0$ measure how difficult it is to prepare the ground state of $H_{XY}^{AFM(FM)}$ by sweeping δ. **d**, Same as **c** but for the gaps along Ω, as shown in **b**. The inset shows a sketch of the expected phase diagrams for $H_{XY}^{AFM(FM)} + H_X$.

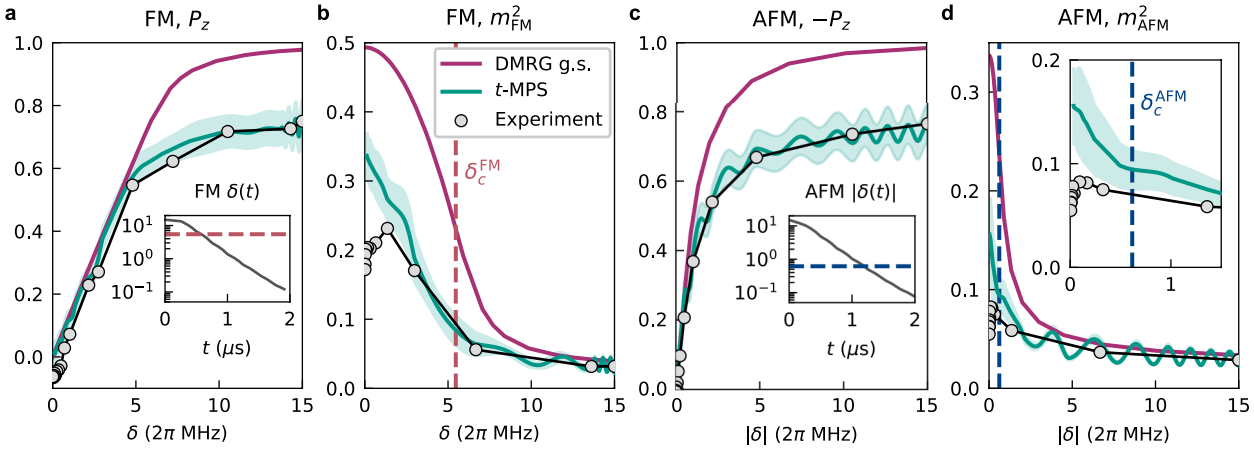

Extended Data Fig. 6 | Numerical simulation of the adiabatic preparation for the 6 × 7 lattice. We compare the predictions from the t-MPS simulations (disorder ensemble average in dark teal, standard deviation in light teal) to the experimental data (grey), as measured at light-shift $\delta(t) = \delta$. We also show the ground-state expectation value from DMRG (purple) **a**, The staggered polarization P_z of the FM. Theory and experiment agree remarkably well, except for an offset at small δ, due to the light-shift-induced depumping. Inset: ramp $\delta(t)$ used for the FM simulation. **b**, The ferromagnetic magnetization $m^2_{FM}(\delta)$. We find excellent agreement between experiment and numerics for $\delta > 2$, including near the phase transition at $\delta_c^{FM} = 5.5$ (red dashed line). The two diverge somewhat at smaller δ (later times), likely due to decoherence and unmodeled systematic measurement errors. **c, d**, Corresponding results for the AFM. For P_z, the t-MPS simulation accurately reproduces the experimental data across the whole $\delta(t)$ sweep. For δ far above $\delta_c^{AFM} = 0.6$ (blue dashed line), there are many-body Rabi oscillations characteristic of the paramagnetic phase. **c**, Inset: ramp $\delta(t)$ used for the AFM simulation. **d**, Inset: zoom-in of lower left corner. At small δ (late times), the magnetization m^2_{AFM} measured in experiment is below that predicted from the simulations.

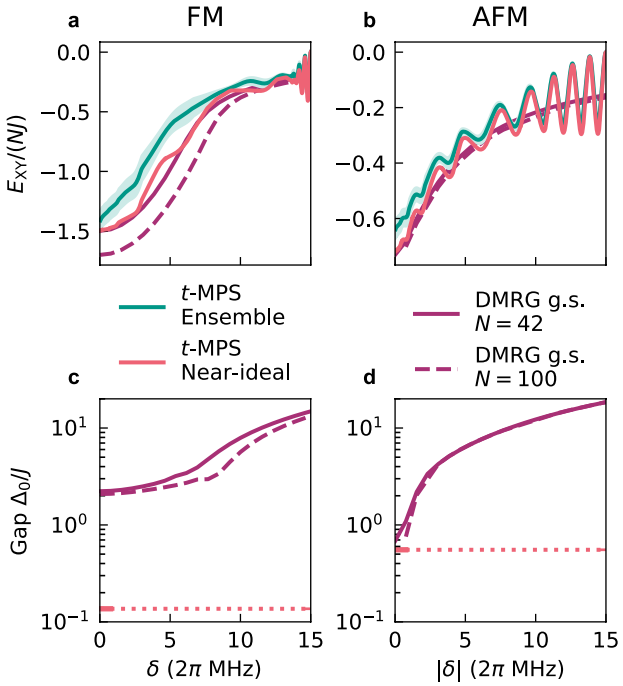

Extended Data Fig. 7 | Energetics of the simulated adiabatic preparation. **a, b**, Interaction energy density $E_{XY}/\overline{N}(\delta)$ in the *t*-MPS simulations of the 6 × 7 lattice. The teal line and envelope are the disorder ensemble average and standard deviation, respectively. Following a single state with minimal initialization errors (pink line), we see that E_{XY} tightly follows the DMRG ground state value (purple), confirming that diabatic errors are negligible. **c, d**, Energy gaps Δ_0 between the ground state and the first excited state in the $S^z = 0$ sector, obtained from DMRG. For the near-ideal initial state, the final energy density (pink dotted line) falls below the gap in both the FM and AFM case.

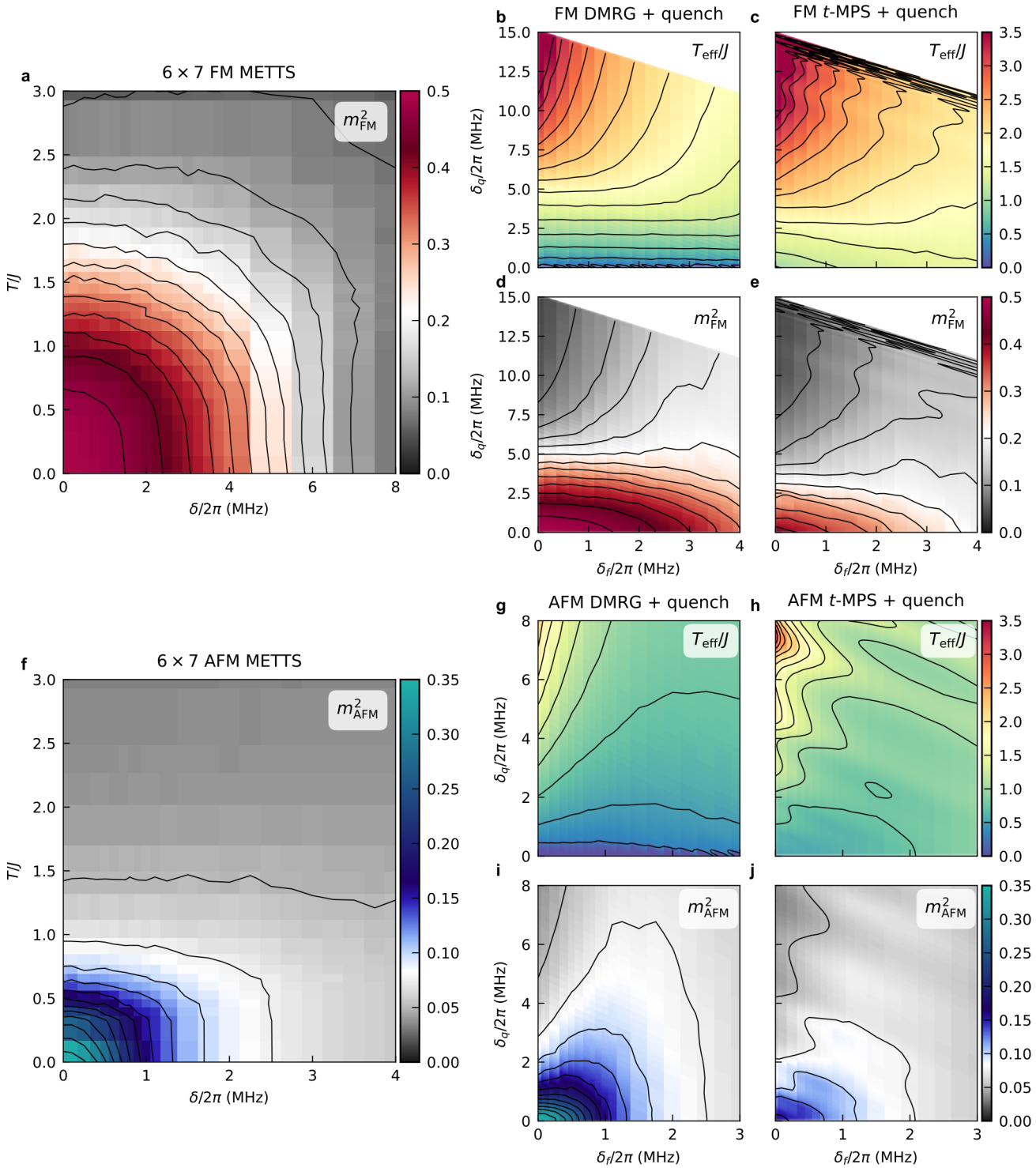

Extended Data Fig. 8 | Finite-temperature properties of $H_{XY} + H_Z$. **a**, Phase diagram of $H^{FM}_{XY} + H_Z$ at finite temperature T and light-shift δ, computed from METTS on a 6×7 array in the $M^z = 0$ sector. We also include $T = 0$ points calculated from DMRG. The region with large magnetization m^2_{FM} at small δ and small T should correspond to the LRO phase in the thermodynamic limit. The colorbar is chosen so that dark red corresponds to the final m^2_{FM} calculated in the t-MPS simulation, absent measurement errors. Thin black lines are equal-magnitude contours to guide the eye. **b,c**, Estimated temperature of a quench experiment with final light-shift δ_f and quench magnitude δ_q, taking the pre-quench configuration to be either the DMRG ground state (**b**) or the t-MPS ramp simulation ensemble (**c**). The oscillatory behavior seen in **c** stems from the paramagnetic Rabi oscillations discussed in Sec. D3. **d, e** Corresponding magnetization m^2_{FM} of the system at temperature $T_{eff}(\delta_f, \delta_q)$. **f-j** Analogous results for the antiferromagnet. The region with finite magnetization m^2_{AFM} is expected to become an algebraic-ordered (BKT) phase in the thermodynamic limit.

Extended Data Table 1 | Summary of the experimental errors defined in Fig. Extended Data 2, together with their main physical origin

Stage	Step	Symbol	Value	Main physical origin
Classical Néel state preparation	Rydberg excitation	η_{STIRAP}	5%	Imperfect optical pumping, Laser phase noise, Spontaneous emission from $6P_{3/2}$ (ref. [54])
	MW π- pulse	η_{MW}	2%	Effect of H_{XY} during pulse
	MW sweep	$\eta_{\mathrm{A}}, \eta_{\mathrm{B}}$	$4\%, 5\%$	Effect of H_{XY} and finite value of $\lvert\delta_0\rvert$
Readout	Freezing	η_{frz}	$< 1\%$	Effect of H_{XY} during pulse
	Deexcitation	η_{dx}	3%	Mechanical effect of deexcitation laser beam
	False $\lvert\downarrow\rangle$	ϵ	1%	Background gas collisions (ref. [54])
	False $\lvert\uparrow\rangle$	ϵ'	5%	Rydberg state radiative lifetime (ref. [54])